Title

Steam-Assisted Selective CO2 Hydrogenation to Ethanol over Ru–In Catalysts

Journal

Angewandte Chemie International Edition, 63(41)

ISSN

1433-7851

Authors

Zhou, Chengshuang

Aitbekova, Aisulu

Liccardo, Gennaro

et al.

Publication Date

2024-10-07

DOI

10.1002/anie.202406761

Selective CO_2 hydrogenation to ethanol over Ru-In catalysts

Chengshuang Zhou[1], Aisulu Aitbekova[2], Michael Stone[1], Eric J. McShane[1], Baraa Werghi[1,3,4], Sindhu Nathan[1], Gennaro Liccardo[1,4], Chengyu Song[5], Jim Ciston[5], Karen C. Bustillo[5], Adam Hoffman[3], Jiyun Hong[3], Jorge Perez-Aguilar[3], Simon Bare[3] and Matteo Cargnello[1,4,*]

[1]*Department of Chemical Engineering, Stanford University, Stanford, California 94305, United States*
[2]*Applied Physics and Materials Science, California Institute of Technology, Pasadena, 91125, CA, USA*
[3]*SLAC National Accelerator Laboratory, 2575 Sand Hill Road, Menlo Park, CA 94025*
[4]*SUNCAT Center for Interface Science and Catalysis, Stanford University, Stanford, CA 94305*
[5]*National Center for Electron Microscopy Facility, Molecular Foundry, Lawrence Berkeley National Lab, Berkeley, CA, 94720, USA*

[*]Corresponding author: mcargnello@stanford.edu

Abstract: Multicomponent catalysts can be designed to synergistically combine reaction intermediates at interfacial active sites, but restructuring makes systematic control and understanding of such dynamics challenging. We here unveil how reducibility and mobility of indium oxide species in Ru-based catalysts crucially control the direct, selective conversion of CO_2 to ethanol. When uncontrolled, reduced indium oxide species occupy the Ru surface, leading to deactivation. With the addition of steam as a mild oxidant and using porous polymer layers to control In mobility, Ru/In interface sites are stabilized, and ethanol can be produced with superior overall selectivity (70%, rest CO) and single-pass yield (6%). Our work highlights how engineering of bifunctional active ensembles enables cooperativity and synergy at tailored interfaces, which unlocks unprecedented performance in heterogeneous catalysts.

An intricate balance in binding energies of different adsorbates on active site ensembles in single-phase catalysts is required to selectively convert reactants into products of interest.[1] Bifunctional catalysts partially relieve these binding energy requirements when reaction intermediates synergistically combine at interfacial active sites,[2] but creating appropriate interactions to drive selective transformations is challenging. To further complicate this challenge, intimacy between active components is crucial to achieve improved performance,[3–5] yet complexity arises from the dynamic nature of active sites,[6–8] and catalyst reconstruction makes systematic control and understanding of such dynamics even harder to achieve.[9–12] Using colloidal particles, we here unveil how dynamics in Ru/In-based catalyst crucially control the direct, selective conversion of CO_2 into ethanol. We demonstrate that the Ru/In interface is highly dynamic and adaptive to the reaction environment due to the reducibility and mobility of indium oxide species. When uncontrolled, reduced indium oxide species occupy the Ru surface, leading to deactivation in C-C coupling and decrease in ethanol production. With the addition of steam as a mild oxidant and using porous polymer layers to control In mobility, the Ru/In interface sites are stabilized, and ethanol can be produced with superior overall selectivity (70%) and single-pass yield (6%). Our work highlights how engineering of bifunctional active ensembles enables cooperativity and synergy at tailored interfaces, which unlocks unprecedented performance in heterogeneous catalysts.

CO_2 hydrogenation to ethanol offers an economically competitive approach for producing a useful chemical building block and fuel which can complement the traditional feedstock-intensive fermentation processes.[13] Additionally, it also has the potential to help relieve our dependence on fossil fuels and to mitigate CO_2 emissions. Ethanol formation on catalytic surfaces requires the intimate colocation of sites that can bind and couple reduced carbon fragments (like $^*CH_3$, where * denotes a surface adsorbate), and oxidized ones (like $^*CO$). Catalysts with sites that strongly favor one of these two common adsorbates produce mostly single-carbon products, such as methane, methanol and CO.[14–16] Ways to improve C-C coupling between carbon adsorbates displaying different oxidation states would lead to the formation of ethanol and other compounds of greater importance and value for a sustainable future.

Multicomponent bifunctional catalysts composed of metals and oxides, such as combinations of Rh-, Ru-, Ni-, Co-based Fischer-Tropsch (FT) catalysts, and In_2O_3- or Cu-based CO_2-to-methanol (CTM) catalysts, have been reported to attempt to combine sites for producing ethanol.[9,17–20] Although evidence suggests that intimacy between these components enhances synergy at interfaces and facilitates rapid transfer of intermediates,[21,22] a correlation between structural intimacy and reactivity is difficult to establish. Direct deposition of FT-active metals on CTM catalysts does not enhance ethanol production,[23–25] yet physical mixtures of similar components leads to enhanced ethanol selectivity.[17,19] Using colloidal Ru particles on In_2O_3-ZrO_2 mixed oxide supports, we here emphasize that the dynamic nature of the catalyst interface is crucial to understand and control the catalytic performance of bifunctional catalysts.

The Dynamic Nature of Ru/In_2O_3-ZrO_2 catalyst

A series of Ru (0.5 wt.%)/In_2O_3 (2.5 wt.%)-ZrO_2 catalysts were prepared either by (i) incipient wetness impregnation (IWI) of a Ru (III) salt or by (ii) colloidal deposition (CD) of 6 nm Ru colloidal particles onto In_2O_3-ZrO_2 oxide support (Fig. S1,2). When tested for CO_2 hydrogenation at 523 K, 6 bar and a H_2:CO_2 ratio of 3:1, the catalyst prepared by IWI method quickly reached steady state, with CO and methanol as the only products, in agreement with previous studies[23,26] (Fig. 1a). The catalyst prepared by the CD method behaved notably differently, and ethanol was initially produced in 9% selectivity (and 6% for methanol, Fig. 1b). The ethanol production, however, decayed rapidly and exponentially with time on stream (Fig. 1b-c) and was replaced by methanol, whose selectivity steadily increased with time (Fig. 1b,d). The methanol production rate at steady state (240 $\mu mol \cdot g_{Ru}^{-1} \cdot s^{-1}$) was roughly 5 times that of the maximum ethanol production rate (46 $\mu mol \cdot g_{Ru}^{-1} \cdot s^{-1}$), likely as a result of three combined factors: (1) methanol could be formed on both Ru-In_2O_3 bifunctional sites and In_2O_3 sites, while ethanol likely could only be produced on the former; (2) ethanol production likely involved different rate limiting steps such as C-C coupling; (3) two moles of CO_2 are converted to produce one mole of ethanol, while only one is required to produce methanol. Simplified first-order rate models (see ***Supplementary Information***) were used to evaluate the evolution of ethanol and methanol production (Fig. 1c-d). It was found that ethanol production (empirical first-order deactivation rate constant $k_{EtOH} = 0.96\ h^{-1}$) strongly and inversely correlated to methanol production ($k_{MeOH} = 1.24\ h^{-1}$). This observation suggests that active sites responsible for ethanol production were initially present in the CD catalyst, but converted on stream into active sites for methanol production. Besides the preparation method, we also studied the effect of other parameters (see Fig S3). It is worth highlighting that catalyst deactivation was strongly correlated with H_2 partial pressure but not CO_2 partial pressure, an indication that coke formation was likely not the cause for deactivation. Carbon balance analysis (Fig S4) further supported this hypothesis. Clearly, knowledge of the structure of the catalyst is

important to understand the cause for the transformation.

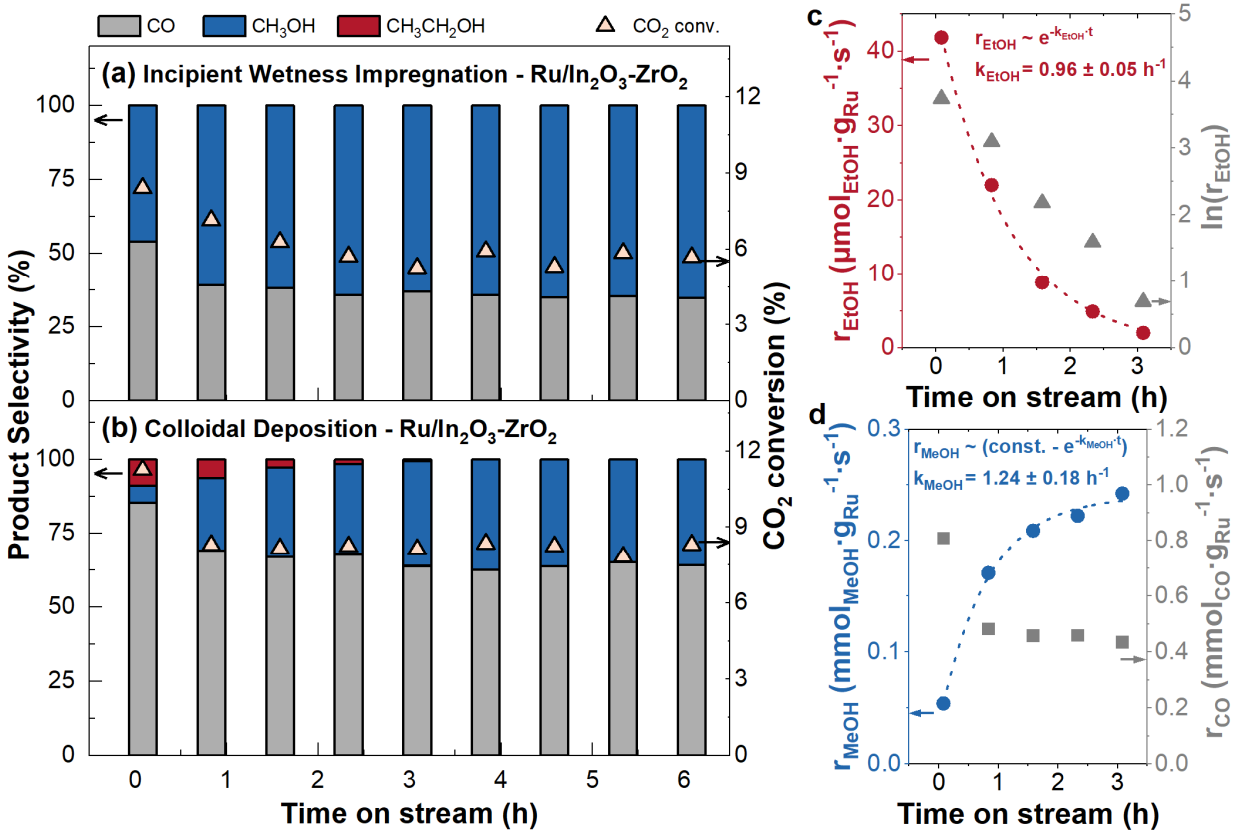

Fig. 1: Distinct catalytic behaviors of Ru-In catalysts. **a,b** CO_2 conversion and product selectivity of (**a**) incipient wetness impregnated (IWI) and (**b**) colloidally deposited (CD) Ru/In_2O_3-ZrO_2 catalysts as a function of time on stream at 523 K, 6 bar, 30 ml·min^{-1} of 3:1 H_2:CO_2. **c** Ethanol production rate of Ru/In_2O_3-ZrO_2 CD catalyst as a function of time (derived from **b**). Dotted line is the fit of ethanol production rate using first-order decay model and k_{EtOH} is the kinetic rate constant. **d** Methanol and CO production rate of Ru/In_2O_3-ZrO_2 CD catalyst as a function of time (derived from **b**). Dotted line is the fit of methanol production rate using self-limiting first-order growth model and k_{MeOH} is the kinetic rate constant.

The Mobility and Reducibility of Indium Species

The structure of the Ru/In_2O_3-ZrO_2 (CD) catalyst was rigorously examined to understand the change in reactivity and deactivation of ethanol production. We chose to analyze the catalyst at time intervals before the reaction (0 minute), when it started to deactivate (5 minutes), and when it had completely deactivated (180 minutes). *Ex-situ* Transmission Electron Microscopy (TEM) analysis of Ru/In_2O_3-ZrO_2 (CD) catalyst at these different stages revealed that Ru colloidal particles (5.8 ± 0.7 nm) retained their size upon deposition onto In_2O_3-ZrO_2 support (5.8 ± 0.9 nm) but became less uniform (5.9 ± 1.9 nm) after 5 minutes of reaction on stream (Fig. S2). After 180 minutes of reaction, Ru particles were found to be notably larger and polydisperse (9.1 ± 4.2 nm) (Fig. S2). Indium species are difficult to differentiate against ZrO_2 supports with TEM due to

similar contrast and Scanning Transmission Electron Microscopy (STEM) and Energy Dispersive X-ray Spectroscopy (EDS) was instead used to understand the distribution of indium species (see Fig S5 for representative EDS spectrum).

By combining *ex-situ* High Angle Annular Dark Field (HAADF)-STEM and EDS mapping characterization, we found that the 0 minute catalyst contained areas where Ru and In were either present individually, or mixed together on the surface of the ZrO_2 support (Fig. 2a-d and Fig. S6). Since Ru and In components were sequentially deposited, it is reasonable that Ru particles and In_2O_3 particles assumed a random distribution on the support. As expected from colloidal synthesis, supported individual Ru nanoparticles can be found with high-resolution (HR)-STEM (Fig. 2e), and the composition was further verified with Electron Energy Loss Spectroscopy (EELS) (Fig 2f). A different picture of the catalyst structure was however obtained for the samples after 5 and 180 minutes of reaction. Rearrangement of the surface species was clearly observed in the 5 minute sample (Fig 2 g-k) and, to a higher degree, after 180 minutes under reaction (Fig 2 m-l), with Ru particles that were found to be fully surrounded by indium species. Fig 2k and 2q are HR-STEM images of representative Ru particles that evidence the presence of a core-shell structure, where amorphous indium oxide species appear to cover the surface of Ru species in the core. Dashed lines were added to guide the eye at the boundaries between high and low contrast regions, whose composition was further verified by the presence of Ru-K and In-M features in the core and shell, respectively (Fig 2 l and r; see additional details on element identification in Fig S7). A prolonged reaction time of 180 minutes did not appear to alter the observed core-shell structure (Fig. 2k and 2q), but the core was observed to have notably grown from 7.6 nm to 12.3 nm (Fig S2). Taken all together, microscopic analysis unambiguously demonstrates that indium species are mobile during the reaction, and they quickly migrate from the ZrO_2 support towards the Ru particles, forming core-shell structures under reaction conditions that are reminiscent of strong metal-support interaction (SMSI) states. [27,28]

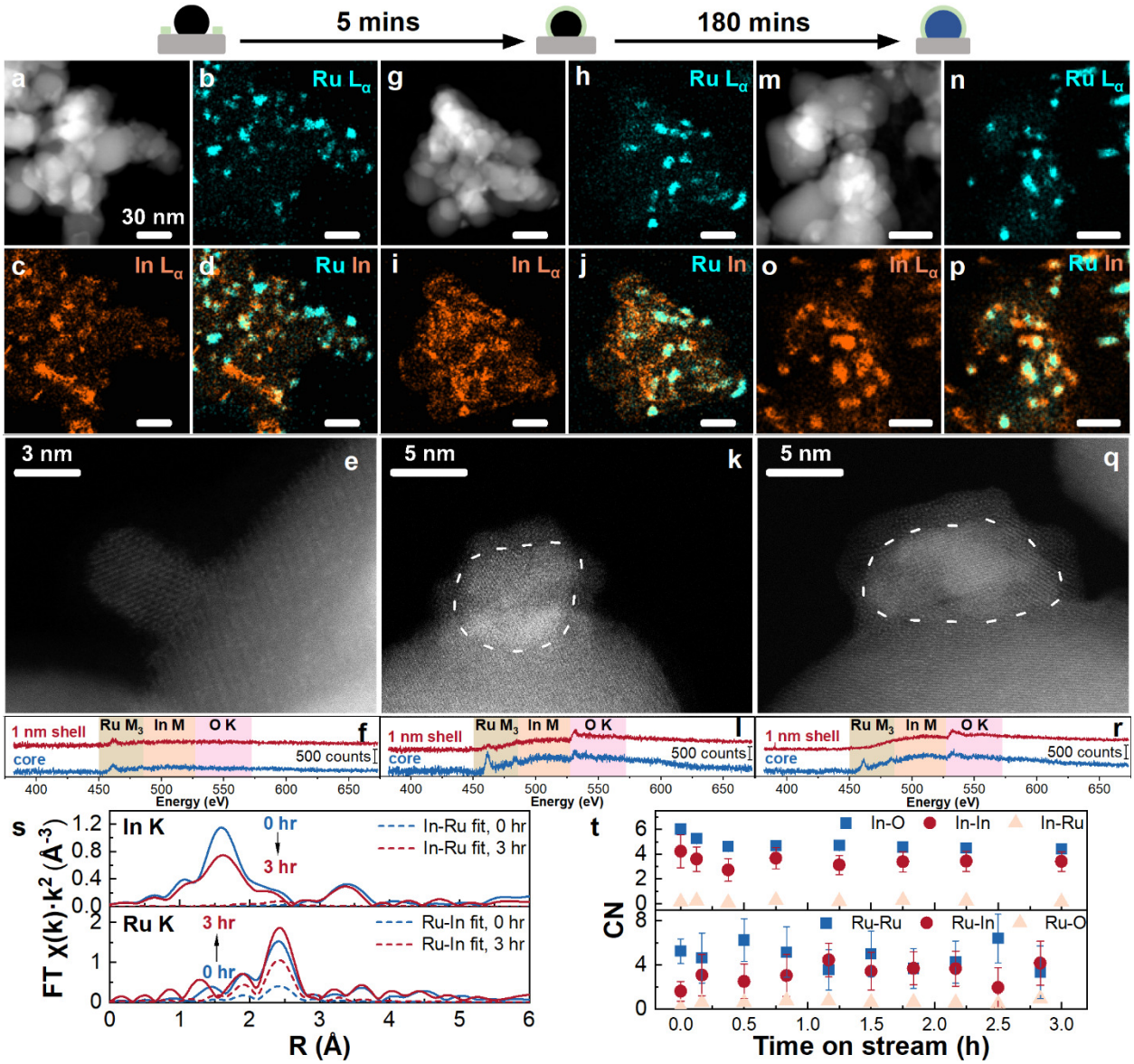

Fig. 2: Characterization of Ru/In_2O_3-ZrO_2 CD catalyst at different stages of reaction. **a,g,m** Representative STEM images, **b-d**,**h-j**,**n-p** Ru L_α and In L_α EDS maps of Ru/In_2O_3-ZrO_2 (CD) catalyst after (**a-d**) 0 minute, (**g-j**) 5 minutes and (**m-p**) 180 minutes of reaction at 523 K, 6 bar, 30 ml·min^{-1} of 3:1 H_2:CO_2. All scale bars are 30 nm unless noted otherwise **e,k,q** Representative HR-STEM images of Ru/In_2O_3-ZrO_2 CD catalyst after (**e**) 0 minute, (**k**) 5 minutes and (**q**) 180 minutes of reaction. **f,l,r** EELS spectra of the catalyst shown in (**e**), (**k**), (**q**) respectively. Dashed lines in (**k**) and (**q**) are intentionally added to highlight the boundary between portions that show different contrasts. Spectra in red were taken from areas that are within 1 nm in depth from the Ru-In_2O_3 ensemble surface, while spectra in blue were from areas that are in the core. Spectra offset for clarity. **(s)** Comparison of Ru-In scattering paths of operando In-K edge and Ru-K edge EXAFS during CO_2 hydrogenation at 523 K, 6 bar, 20 ml·min^{-1} of 3:1 H_2:CO_2. Solid traces are experimental data and dotted traces are fitted Ru-In scattering paths. **(t)** summary of fitted In-O,

In-In, In-Ru, Ru-Ru, Ru-In and Ru-O coordination numbers as a function of time on stream during CO_2 hydrogenation at 523 K, 6 bar, 20 ml·min^{-1} of 3:1 H_2:CO_2.

It is however worth noting that ex-situ microscopy analysis only revealed the distribution of Ru and In species, whose chemical states during CO_2 hydrogenation require *operando* techniques to be characterized. Thus, *operando* XAS was used to interrogate the chemical state of Ru and In species and unveil the driving force responsible for the structural transformation (Fig. 2s,t, Fig. S8-10 and Table S1-3). When examining the In K-edge, a decrease in intensity in the Fourier-transform at peaks centered at 2 Å and 3.2 Å was found as the reaction proceeded (Fig. 2s). This decrease can be attributed to the reduction of In (III), the formation of oxygen vacancies and the decrease in crystallinity of indium oxide particles.[29] The Ru K-edge showed instead an increase in amplitude, in line with the observed core-shell growth and particle enlargement process evidenced by HAADF-STEM (Fig. 2o). By fitting the Ru K-edge and using different potential scattering patterns (Ru-O, Ru-Ru and Ru-In), we were able to identify that the amplitude increase was mainly due to the formation of metallic Ru-In alloy species (~40% of Ru total coordination). See Fig S10 and table S3 for additional information on the identification of Ru-In scattering path.

The coordination numbers for hypothesized In and Ru species at different stages allowed us to evaluate the rate of In_2O_3 reduction and Ru-In alloy formation (Fig. 2t and Table S1,2). The decrease of In-O, In-In, Ru-Ru and the increase of Ru-In coordination numbers occurred rapidly within the first 30 mins, which qualitatively agreed with the rapid deactivation in ethanol production (Fig. 1), and the rapid increase in methanol production (Fig. S9e). We postulate that upon the initial contact of reactants on stream, Ru particles dissociate hydrogen and catalyze the reduction of indium oxide species, which quickly migrate towards Ru and eventually encapsulate it, forming the core-shell Ru@In_2O_{3-x} structure (*x* denotes the fraction of oxygen vacancies that result from indium oxide reduction). The structural change did not stop until interfacial indium was slowly and sequentially further reduced to a metallic state and alloyed to the Ru core, overall leading to the formation of Ru-In alloys surrounded by partially reduced indium oxide species (Ru-In@In_2O_{3-x}).

Catalysts based on metallic In alloys reported in the literature, including Ru-In[26], Pd-In[30] and Ni-In[25], have been described to produce only methanol and to not perform C-C coupling. Indium likely occupies the surface or subsurface sites in these alloy systems,[31] which prohibits CO adsorption and dissociation and limits C-C coupling and therefore ethanol production. To correlate the observed structure evolution to the reactivity changes, we propose that the active phase for ethanol production is a Ru-In_2O_3 interface structure that is quickly formed *in-situ*, while the excessive reduction of indium and the formation of Ru-In alloys lead to methanol formation. It is worth mentioning that the reason that Ru/In_2O_3-ZrO_2 catalyst prepared with IWI method did not, even transiently, produce ethanol is likely because Ru was highly dispersed and Ru-In ensembles were already formed during the synthesis of such catalyst (Fig. S1), which helps explain why there is no precedent in the literature of using these alloys for ethanol production.

Steam Stabilizes Ru-In_2O_3 Interfaces

We propose that regulating the degree of indium oxide reduction, while leaving Ru in its metallic state, is the key to stabilizing the intermediate Ru-In_2O_{3-x} interface structure and ethanol production. The challenge is that the highly reducing chemical potential under CO_2 hydrogenation conditions strongly promotes deep reduction of In species. Specifically, although CO_2 is a weak oxidizer, it alone could not efficiently regulate the chemical state of indium, as demonstrated by temperature-programmed oxidation experiments in Fig S11. We invoke that the introduction of H_2O (steam) allows for the regulation of indium reduction through Le Chatelier's principle, since the reverse reaction of In_2O_3 reduction, which is the oxidation of metallic indium by water, is kinetically feasible at the relevant conditions for ethanol production.[32] It is also worth mentioning that the addition of steam is not expected to interfere with the thermodynamic distribution of products.[33] When 5% steam was used as a mild oxidant, hydrogen was generated from a deactivated Ru/In_2O_3-ZrO_2 CD catalyst, but not from a Ru/ZrO_2 CD catalyst, indicating that In was selectively oxidized by steam (Fig. 3a). We further evaluated the effect of the concentration of added steam on the ethanol production (Fig. 3b). The introduction of steam readily decreased the deactivation rate of ethanol production and prolonged the half-life of the catalyst. 10% steam was the optimum concentration value under our conditions. It is likely that excess amounts of steam either compete with CO_2 hydrogenation or promote structural transformations that lead to In immobility.

The addition of 10% steam enabled us to investigate the structure of the catalyst that produced ethanol at a steady rate. *Ex-situ* STEM-EDS showed that aggregation of Ru and In species could still be discerned after 180 minutes of reaction (Fig. 3c-f), suggesting that the mobility of indium species was not completely avoided, a crucial aspect for the *in-situ* formation of Ru-In_2O_{3-x} active interfaces. HR-STEM revealed that 10% steam, however, dramatically changed the structure of these ensembles (Fig. 3g), demonstrating that the Ru particles remained mostly unchanged in size and morphology compared to the initial catalyst state (see also Fig. S2). Only a thin layer of indium oxide was found to partially decorate the Ru surface by EELS analysis (Fig. 3h). *Operando* XAS (Fig 3i,j, Fig S12,13 and Table S4,5) revealed that a minor decrease (10%) in the In-O shell contribution intensity was found through In K-edge analysis in the catalyst tested with 10% steam (Fig. 3i). Ru K-edge remained identical for 180 minutes of reaction (Fig. 3i). Besides a minor decrease in the In-O coordination number within the first hour (from 5.8 ± 0.2 to 5.4 ± 0.1), In-In and In-Ru coordination numbers remained stable around 5.1 ± 0.1 and 0.2 ± 0.1, respectively, indicating no major changes in the In environment. At the same time, Ru-Ru coordination numbers remained constant at 8.1 ± 1.2, while Ru-In interactions (0.1 ± 0.8), likely present at the Ru-In interface, only accounted for 1% contribution to the total Ru coordination numbers (Fig. 3j). Meanwhile, deactivation in ethanol production was not discerned during *operando* XAS experiments (Fig. S12e). All evidence suggests that In_2O_3 remained stable, Ru remained mostly metallic, and that Ru-In alloys were not formed. We conclude that Ru-In_2O_{3-x} interfaces with a controlled reduction are the active site ensemble necessary for ethanol production.

In-situ DRIFTS during CO_2 hydrogenation revealed the uniqueness of such spatial and compositional arrangements of Ru and In species. Under CO_2 hydrogenation conditions at 6 bar without steam, three main adsorption bands were detected. Extrapolating from relevant studies on Ru-Sn catalysts[34], we attributed the three bands to *CO adsorbed on oxidized Ru at the Ru-In_2O_3

interface (2051 cm^{-1}), *CO adsorbed on metallic Ru in Ru-In alloys (2007 cm^{-1}), and *$(CO)_2$ adsorbed on Ru-In alloy sites (1963 cm^{-1}) (Fig 3k). Although the exclusive presence of Ru-In sites reflected the intimacy between In and Ru species, ethanol was likely not produced from these sites, as it would be unlikely for intermediate *CO species to dissociate or couple, due to the lack of Ru-Ru neighboring sites.[34] C_1 oxygenates like CO and methanol would be the only products of such structures (Fig 1a). Instead, with 10% additional steam to preserve the Ru-In_2O_3 interface, one additional bridged *CO adsorbed on Ru-Ru sites (1828 - 1921 cm^{-1}), which is crucial for *CO dissociation and C-C coupling, was detected (Fig. 3k). Since the presence of Ru-Ru sites is inversely correlated to the fraction of Ru-In alloys formed, it is reasonable that they can only be found in Ru-In_2O_3 ensembles stabilized by steam. These observations further reinforce our hypothesis that the intimacy between In_2O_3 and Ru ensures a rapid transfer of intermediates, so that ethanol is produced from the coupling events on Ru-Ru sites at the Ru-In_2O_3 interface.

To summarize, synergistic effects from Ru and In_2O_3 that overcome linear scaling require stable and intimate Ru-In_2O_3 interfaces, whereas incorporation of metallic indium deactivates Ru for ethanol production. This reduction of indium could either occur unintentionally from the reductive pre-treatments usually conducted on IWI catalysts, or from *in-situ* reduction by the CO_2 hydrogenation reaction mixture, both leading to the formation of Ru-In alloy (Fig. 3l). The addition of steam regulates the In_2O_3 reducibility, preventing excessive reduction and maintaining the Ru-In_2O_3 interface, which is the active phase for ethanol production.

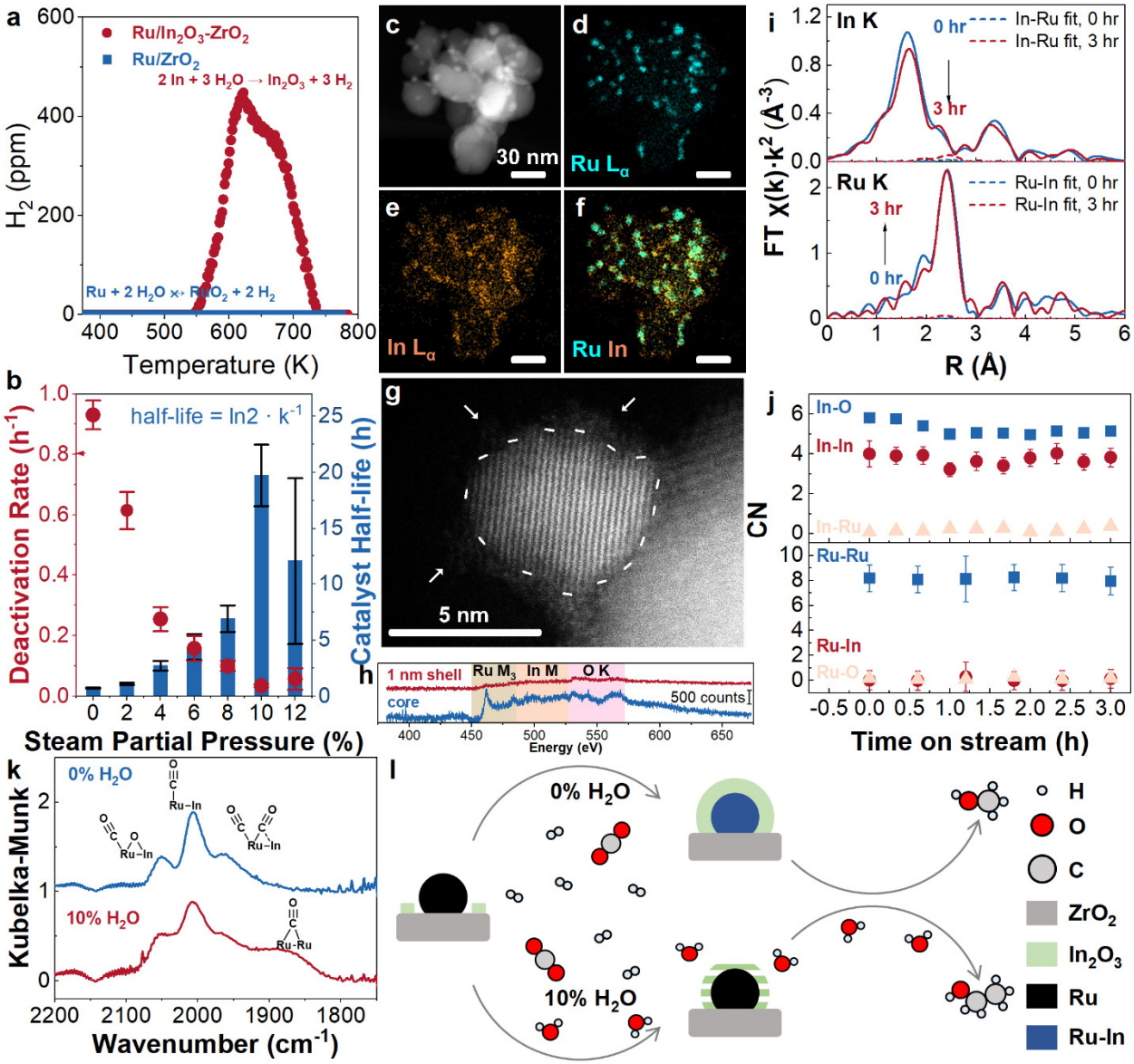

Fig. 3: The addition of steam stabilizes Ru-In_2O_3 interface for ethanol production. **a** Hydrogen evolution as the result of metal re-oxidation by 5% steam during temperature-programmed-oxidation (TPO) experiment. Catalysts were previously intentionally deactivated by H_2 reduction at 673 K **b** Effect of steam concentration on the deactivation rate and half-life of Ru/In_2O_3-ZrO_2 CD catalyst for CO_2 hydrogenation at 523 K, 6 bar, 30 ml·min^{-1} of 3:1 H_2:CO_2 and steam. **c** Representative STEM image, **d-f** Ru L_α and In L_α EDS maps, **g** representative HR-STEM image and **h** EELS spectra of Ru/In_2O_3-ZrO_2 (CD) catalyst after 180 minutes of reaction at 498 K, 6 bar, 30 ml·min^{-1} of 3:1 H_2:CO_2 and 10% steam. EELS spectra in red were taken from areas that are within 1 nm depth from the Ru-In_2O_3 ensemble surface, while spectra in blue were from areas that are in the core. **i** Comparison of Ru-In scattering paths of *operando* In-K edge and Ru-K edge EXAFS at 498 K, 6 bar, 20 ml·min^{-1} of 3:1 H_2:CO_2 and 10% steam. Solid traces are experimental data and dotted traces are fitted Ru-In scattering paths. **j** summary of fitted In-O, In-In, In-Ru, Ru-

Ru, Ru-In and Ru-O coordination numbers as a function of time on stream. **k** CO-adsorption region of the *in-situ* DRIFTS spectra of Ru/In_2O_3-ZrO_2 (CD) catalyst during CO_2 hydrogenation at 498 K, 6 bar, 30 ml·min^{-1} of 3:1 H_2:CO_2, without (blue) or with (red) added 10% steam. **i** Schematic illustration of structural evolution of Ru/In_2O_3-ZrO_2 CD catalyst.

Stable and Selective Ethanol Production

In previous work, we demonstrated that encapsulation of supported metal catalysts within porous organic polymers leads to increased C-C coupling probability during CO_2 hydrogenation on Ru/TiO_2 catalysts.[35] We hypothesized that the polymer layers could have a similar function in the current system and further enhance the performance of the Ru-In_2O_3 interface.[35] Hence, we encapsulated the Ru/In_2O_3-ZrO_2 catalyst within an imine-based porous organic polymer (IPOP) layer (Fig S14). Uniform polymer layers can be found encapsulating Ru/In_2O_3-ZrO_2 catalyst, with Ru particles being still distinguishable (Fig 4a). The encapsulation indeed effectively enhanced ethanol selectivity and catalyst stability even without additional steam (Fig S15). The catalyst remained structurally intact when 10% steam was added, and neither morphological changes (Fig 4d) nor compositional changes (Fig. S14,16,17 and Table S6,7) could be discerned after 24 hours of reaction at 498 K, 6 bar, 30 ml·min^{-1} of 3:1 H_2:CO_2 and 10% steam.

Reaction conditions including temperature, pressure, WHSV and reactant ratio were then studied and optimized (Fig S18). We report here that under optimized conditions, this catalyst system showed 70% ethanol selectivity (with 30% CO as the only by-product) at 8% conversion from steam-assisted CO_2 direct hydrogenation (Fig 4b). The performance of this IPOP/Ru/In_2O_3-ZrO_2 is superior to all reports in this field (see comparision in Table S8), and only slightly decreased after 24 hours on stream (Fig 4c). It is also worth noting that albeit slight deactivation, no by-products other than CO were detected.

Overall, for the first time, we report the discovery of near-exclusive ethanol production on Ru/In_2O_3-ZrO_2 catalysts. The encapsulation of metallic ruthenium by In_2O_3 facilitates a rapid transfer of reaction intermediates, maximizing the synergy at the Ru-In_2O_3 interfacial sites, which lays a strong foundation for the systematic understanding of CO_2 direct hydrogenation into C_{2+} oxygenates. We also wish to highlight that the traditional impregnation-calcination-reduction approaches could overlook transient active sites formed during the synthesis steps. Colloidal approaches help uncover unexpected findings as they provide better control and precise understanding of the initial state of as-synthesized catalysts. This work provides a novel way to design multifunctional catalysts to circumvent linear scaling for chemical production with unprecedented activity and selectivity.

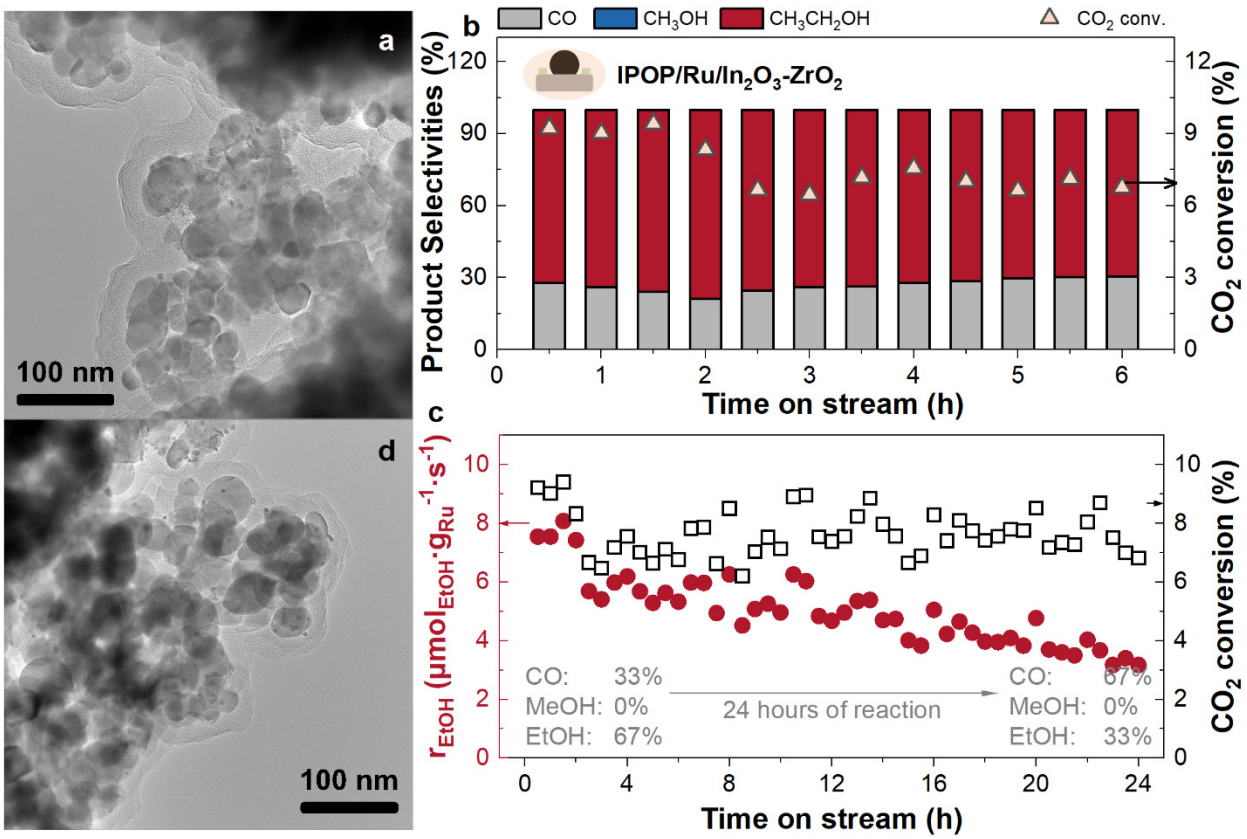

Fig. 4. Stable and selective ethanol production with IPOP/Ru/In_2O_3-ZrO_2 CD catalyst from steam-assisted CO_2 hydrogenation. **(a,d)** Representative TEM images of IPOP/Ru/In_2O_3-ZrO_2 catalyst (**a**) as-synthesized and (**d**) after 24 hours of reaction at 498 K, 6 bar, 30 ml·min^{-1} of 3:1 H_2:CO_2 and 10% steam. **(b)** CO_2 conversion and product selectivity of IPOP/Ru/In_2O_3-ZrO_2 catalyst in the first 6 hours of catalysis test at 498 K, 6 bar, 20 ml·min^{-1} of 3:1 H_2:CO_2 and 10% steam. **(c)** CO_2 conversion and ethanol production rate of IPOP/Ru/In_2O_3-ZrO_2 catalyst as a function of time during 24 hours of continuous test at 498 K, 6 bar, 30 ml·min^{-1} of 3:1 H_2:CO_2 and 10% steam. Selectivity for all products at the 1st and 24th hour of reaction is also provided in (**c**).

Methods

Catalyst preparation

Preparation of In_2O_3-ZrO_2 oxide

In_2O_3-ZrO_2 oxide supports were prepared using incipient wetness impregnation of $In(NO_3)_3 \cdot xH_2O$ (Sigma, x was determined to be 5 from TGA analysis.) Note that this chemical is hygroscopic, and we recommend measuring the degree of hydration before use. Typically, $In(NO_3)_3 \cdot xH_2O$ (65.5 mg on anhydrous basis) was dissolved in 1 mL of ethanol and added dropwise onto 1 g of ZrO_2 on a glass petri dish. A glass rod was used to break down aggregations of ZrO_2 and to gently mix the powder. The sample was then dried at 353 K overnight, transferred into an alumina crucible and calcined in static air at 873K for 2 hours using a ramp rate of 5 $K \cdot min^{-1}$ to obtain 2.5 wt.% In_2O_3-ZrO_2.

Preparation of Ru/In_2O_3-ZrO_2 IWI catalyst

Ru was deposited on In_2O_3-ZrO_2 support via the incipient wetness impregnation of $Ru(NO)(NO_3)_3$ (Sigma) in an aqueous solution, targeting a 0.5 wt% Ru loading. Typically, 15.7 mg of $Ru(NO)(NO_3)_3$ was dissolved in 1 mL of water, and added dropwise onto 1 g of ZrO_2 on a glass petri dish. A glass rod was used to break down aggregations of ZrO_2 and to gently mix the powder. The sample was dried at 353 K overnight, transferred into an alumina crucible and calcined in static air at 583 K for 5 hours with a ramp rate of 5 $K \cdot min^{-1}$. The sample was then reduced in a tube furnace under a flow of 30 $ml \cdot min^{-1}$ 5% H_2 for 2 hours at 523 K with a ramp rate of 10 $K \cdot min^{-1}$.

Preparation of Ru/In_2O_3-ZrO_2 CD catalyst

6 nm colloidal Ru nanoparticles were prepared by thermal decomposition of $Ru_3(CO)_{12}$ via colloidal synthesis using standard Schlenk techniques. Briefly, 32 mL of oleylamine (OLAM, 70%) was added to 160 mg of $Ru_3(CO)_{12}$ (99%, Sigma-Aldrich) in a three-neck flask. The reaction content was degassed (<2 Torr) for 30 min at room temperature. The flask was then flushed with nitrogen, heated to 543 K at a rate of ~20 $K \cdot min^{-1}$ and kept at this temperature for 30 minutes before cooling down to RT. The particles were purified by precipitation with ethanol (total volume 30 ml) followed by centrifugation (8000 rpm, 3 min) and redissolution in hexanes for three times, and finally dispersed in hexanes. The concentration of Ru in this hexanes suspension was measured by TGA analysis.

Targeting at 0.5 wt% Ru, 5mg of Ru nanoparticles in hexanes were added dropwise into a suspension of 1 g In_2O_3-ZrO_2 in 100 ml hexanes under vigorous stirring. The mixture was allowed to stir for 30 minutes once all Ru was added. The catalysts were collected by centrifugation at 8000 rpm for 3 mins, dried at 353 K overnight, and thermally treated for 30 s at 973 K in an air furnace to remove organic ligands.

Preparation of IPOP/Ru/In_2O_3-ZrO_2 CD catalyst

Polymer encapsulation was adapted from our previous work.[35] 450 mg of Ru/In_2O_3-ZrO_2 CD catalyst together with 88 mg of benzene-1,3,5-tricarboxaldehyde and 88 mg of p-

phenylenediamine were added into 24 mL of 1,4-dioxane and sonicated for 5 min until full dispersion/dissolution. The solution was further stirred for 30 min under room temperature to promote adsorption of organic monomers and oligomers onto inorganic substrates. 0.6 mL of acetic acid was then added as Brønsted acid catalyst for imine condensation. The polymerization was allowed to proceed for 90 min, after which products were collected by centrifugation and subsequently washed with methanol and filtered for 3 rounds. The samples were finally dried at 353K under dynamic vacuum conditions for 12 hours.

Catalyst characterization

TEM

Bright-field transmission electron microscopy (TEM) images were collected using an FEI Titan ETEM instrument at 300 kV. The samples were suspended in isopropyl alcohol and drop casted onto ultrathin lacey carbon supported on a 400-mesh nickel grid for all measurements.

HAADF-STEM-EDS

High angle annular dark-field scanning transmission electron microscopy (HAADF-STEM) images and energy dispersive spectroscopy maps (EDS mapping) were acquired using a FEI TitanX equipped with SuperEDS detector at 300 kV at the National Center for Electron Microscopy (NCEM) at the Lawrence Berkeley National Laboratory (LBNL). Map acquisition was typically ~ 5 min at a beam current of 330 pA. Samples were prepared for analysis by dispersing the powder on lacey C/Cu grids by shaking a small amount of powder sample with a TEM grid in a small scintillation vial. Bruker Esprit 1.9 software was used to process and quantify the EDS maps using the following approach. First, a fit of the Brems-strahlung background X-rays was subtracted from the hyperspectral images using pre-defined fitting regions where no characteristic X-ray peaks appeared. Corrections for escape peaks, pileup peaks, shelf, tail, and shift errors were applied. Since Ru and In atomic concentrations are far lower than ZrO_2, a peak deconvolution routine was used to remove any contribution from Zr L-edge to Ru and In L-edges. Figure S11 shows a typical spectrum from the summed pixels in a map.

STEM-EELS

HAADF-STEM-EELS data were collected at the Molecular Foundry on the TEAM I instrument, which is a double-corrected transmission electron microscope on the Thermo Fisher Titan platform with a Gatan Continuum GIF. HAADF-STEM images were collected at 300kV with a convergence semiangle of 17 mrad and a collection angle of 110-400 mrad and 15 microseconds per pixel dwell time. Electron energy loss spectra were recorded on a post-GIF K3 detector in electron counting mode with a dispersion of 0.18 eV per pixel. Spectrum images were acquired using an 80 pA probe current, a 50 ms dwell time and 2 nm pixels with 16×16 sub-scanning of each STEM pixel. The spectrometer was operated in dual-EELS mode to recorded both the elastic (zero-loss) and core-loss portion of the spectrum. ZLP-lock processing engaged during acquisition to dynamically correct shifts in the zero-loss energy before summation of individual electron-counted spectral. A power-law background was subtracted from summed spectra using a window of at least 50 eV below the Ru M-edge. EELS map data processing method can be found in Fig S7 for details.

Operando XAS

Operando X-ray absorption measurements at Ru K-edge (11.564 keV) and In K-edge (27.940 keV) were performed at beamline 9-3 of the Stanford Synchrotron Radiation Lightsource at the SLAC National Laboratory. Beamline 9–3 is a 16-pole, 2-tesla wiggler beamline with a vertically collimating mirror for harmonic rejection and a cylindrically bent mirror for focusing. Incident photon energy was selected by the liquid-nitrogen cooled, double-crystal Si(220) monochromator at crystal orientation of = 90. The catalyst sample was pressed, crushed, and sized between 80 and 120 mesh sieves. Approximately 70 mg of the sieved sample was loaded to make a 9-mm bed in a 3-mm quartz tube, held in place by two plugs of quartz wool. The capillary was loaded into a custom-built flow-reactor reactor. The reactor was mounted on the sample stage at a 45° angle relative to the X-ray beam. Spectra were collected in fluorescence detection mode, with Ge detector orthogonal (90°) to the beam path with a 10-cm Soller slit for Ru-K edge and PIPS detector for In-K edge. The beam size of 1 mm [v] by 3 mm [h] was used. Ar-filled ion chambers were used to measure the incident X-ray intensity and the Ru foil and In foil reference, which was scanned simultaneously with the sample for energy calibration. Gas flow rates were controlled using mass flow controllers (Brooks) and temperature was controlled with a Eurotherm PID controller. To monitor the gas flows, a mass-spectrometer (Hiden QGA) was used throughout the experiment. During each experiment, catalysts were first heated to desired temperatures in a flow of 20 ml/min He, then pressurized to 6 bar. 4 EXAFS scans were collected and used to represent the initial (0 min) state of the catalyst. EXAFS scans were then continuously collected while gas flow was switched to 3:1 H_2:CO_2. For steam-assisted experiments, 10% steam was also introduced with a stainless-steel saturator, and gas components were also analyzed with Agilent 8890 GC system. Experiments were always performed with fresh catalysts for both Ru-K and In-K edge.

The XAS data was processed using the Athena software of the Demeter package. The EXAFS spectra were energy calibrated, merged, and normalized. In-K scans were merged in groups of 10, while Ru-K was not merged. The normalized EXAFS spectra were modeled using the Artemis software of the Demeter package.

S_0^2 was calculated to be 0.76 ± 0.06 by fitting Ru foil, and 0.98 ± 0.09 In foil. For modelling EXAFS of different states, scattering paths generated from Ru_mp-33.cif, RuO_2_mp825.cif, In_2O_3_mp-22598.cif and $RuIn_3$_mp-607450.cif from the materials project were used. EXAFS from different time-on-stream within same experiment were analyzed and fit together, sharing ΔE_0, reduced chi^2 and R factors. Additionally, same paths from different spectra share identical R and σ^2.

TPO

Temperature-programmed-oxidation (TPO) experiments were conducted under atmospheric pressure in a U-shaped quartz glass reactor with a 1-cm inner diameter using 150–200 mg of catalyst powder. The catalyst bed temperature was measured using a K-type thermocouple inserted into the middle of the reactor bed. Prior to the experiment, catalysts were reduced at 673 K with 40 ml·min^{-1} 5% H_2 for 2 hours. Under 30 ml·min^{-1} 5% H_2O balanced with Ar, the reactor was

heated at 6 K/min from 373 to 773 K. Gas composition was analyzed with a mass-spectrometer (Hiden QGA).

DRIFTS

Diffuse Reflectance Infrared Fourier Transform Spectroscopy (DRIFTS) was performed in a Praying Mantis DRIFTS system (Harrick). Samples were loaded into a high temperature and pressure reaction cell with ZnSe windows. Gas flow rates were controlled using EL-Flow series mass flow controllers (Bronkhorst). Background spectra was acquired at 498 K with KBr under N_2 flow. For in-situ CO_2 hydrogenation measurements without steam, feed gas consisted of 30 $ml \cdot min^{-1}$ N_2 was introduced, and the sample cell was gradually pressurized and heated. Once at 6 bar and 498 K, the feed gas was then switched to 30 $ml \cdot min^{-1}$ 3:1 H_2:CO_2. IR spectra were collected throughout the sample treatment process using a Bruker Vertex 70 spectrometer with a liquid nitrogen-cooled mercury-cadmium-telluride (MCT) detector. Each spectrum was measured by averaging 200 scans over the range 600-4400 cm^{-1}. For CO_2 hydrogenation measurements with steam while avoiding potential corrosion of ZnSe window by high-temperature steam, the catalyst was allowed to react ex-situ at 498 K under 6 bar and 30 $ml \cdot min^{-1}$ 3:1 H_2:CO_2 with 10% steam for 1 hour, and transferred to IR instrument under the protection of Ar. IR spectra were collected immediately.

Reactivity Measurements

Catalytic experiments were conducted in a custom-made stainless-steel reactor with an internal diameter of 1 cm. Approximately 0.2 g – 1.0 g of catalysts were loaded into the reactor in between two layers of granular acid-washed quartz. The amount of catalyst was adjusted to make sure conversions were below 10% unless noted otherwise. No pretreatments were performed prior to reaction, and catalysts were carefully brought to reaction conditions while minimizing the exposure to any environments that might lead to compositional or structural changes. Specifically, the reactor was heated to reaction temperature (523 or 498 K) under 40 $ml \cdot min^{-1}$ Ar. The feed gas was then switched to 40 $ml \cdot min^{-1}$ 3:1 H_2:CO_2 and the reactor was gradually pressurized to 6 bar for ~10 minutes. Once at 6 bar, the flow rate of feed gas was reduced to 30 $ml \cdot min^{-1}$. All products remained in the gaseous phase and thus continuously analyzed by a Gas Chromatography (GC) system (SRI MG5) equipped with a Hayesep D column. GC analysis was initiated 5 minutes after pressure reached 6 bar. CO, methanol and ethanol were quantified using flame ionization detector, while H_2 and CO_2 consumption was measured using thermal conductivity detector. Additional steam was introduced to the reactor with a stainless-steel H_2O-saturator for steam-assisted CO_2 hydrogenation experiments. Similarly, after catalyst loading, the reactor was heated to 498 K under 40 $ml \cdot min^{-1}$ Ar. Reaction mixture (40 $ml \cdot min^{-1}$ 3:1 H_2:CO_2) was mixed upstream of the saturator, introduced to the H_2O saturator heated to different temperatures, and eventually introduced to the reactor, carrying different partial pressures of steam. Steam pressure was calculated with Antoine formula. For 10 % steam at 6 bar, the saturator was heated to 359 K (saturation vapor pressure = 0.6 bar).

CO_2 conversion was calculated by the equation:

$$CO_2\ conversion\ (\%) = \frac{CO_{2_{in}} - CO_{2_{out}}}{CO_{2_{in}}} \cdot 100\%$$

Where CO_2 (in) and CO_2 (out) denote moles of CO_2 at the inlet and outlet, respectively.

Selectivity distribution of individual products was calculated by equation:

$$C_xH_yO_z\ Selectivity\ (\%) = \frac{x \cdot C_xH_yO_{z_{out}}}{CO_{2_{in}} - CO_{2_{out}}} \cdot 100\%$$

Where $C_xH_yO_z$ denote moles of possible products, such as CO, CH_3OH and C_2H_5OH in the outlet.

Acknowledgements

This work was supported by the Packard Foundation. Additional support was provided by a seed grant from the Precourt Institute of Energy at Stanford University. M. C. acknowledges support from a Sloan Fellowship, as well as the Novo Nordisk Center for CO_2 Research. E.J.M. and M.C. acknowledge funding from the Villum foundation V-SUSTAIN Grant 9455. Part of this work was performed at the Stanford Nano Shared Facilities, supported by the NSF under award ECCS-1542152. Work at the Molecular Foundry was supported by the Office of Science, Office of Basic Energy Sciences, of the US Department of Energy under contract DE-AC02-05CH11231. The synchrotron work was performed at Stanford Synchrotron Radiation Lightsource (SSRL) of SLAC National Accelerator Laboratory and use of the SSRL is supported by the US Department of Energy, Office of Science, Office of Basic Energy Sciences under contract DE-AC02-76SF00515. Dr. Melissa Cendejas and Sarah Edwards are acknowledged for their help with XAS experiments.

References

1. Nørskov, J. K. *et al.* Universality in Heterogeneous Catalysis. *Journal of Catalysis* **209**, 275–278 (2002).
2. Pérez-Ramírez, J. & López, N. Strategies to break linear scaling relationships. *Nat Catal* (2019) doi:10.1038/s41929-019-0376-6.
3. Zecevic, J., Vanbutsele, G., de Jong, K. P. & Martens, J. A. Nanoscale intimacy in bifunctional catalysts for selective conversion of hydrocarbons. *Nature* **528**, 245–248 (2015).
4. Zabilskiy, M. *et al.* The unique interplay between copper and zinc during catalytic carbon dioxide hydrogenation to methanol. *Nat Commun* **11**, 2409 (2020).

5. Zhang, J. *et al.* Origin of synergistic effects in bicomponent cobalt oxide-platinum catalysts for selective hydrogenation reaction. *Nat Commun* **10**, 4166 (2019).
6. Frey, H., Beck, A., Huang, X., van Bokhoven, J. A. & Willinger, M. G. Dynamic interplay between metal nanoparticles and oxide support under redox conditions. *Science* **376**, 982–987 (2022).
7. Beck, A. *et al.* Following the structure of copper-zinc-alumina across the pressure gap in carbon dioxide hydrogenation. *Nat Catal* **4**, 488–497 (2021).
8. Behrens, M. *et al.* The Active Site of Methanol Synthesis over $Cu/ZnO/Al_2O_3$ Industrial Catalysts. *Science* **336**, 893–897 (2012).
9. Caparrós, F. J. *et al.* Remarkable Carbon Dioxide Hydrogenation to Ethanol on a Palladium/Iron Oxide Single-Atom Catalyst. *ChemCatChem* **10**, 2365–2369 (2018).
10. Goodman, E. D. *et al.* Catalyst deactivation via decomposition into single atoms and the role of metal loading. *Nat Catal* **2**, 748–755 (2019).
11. Aitbekova, A. *et al.* Low-Temperature Restructuring of CeO_2-Supported Ru Nanoparticles Determines Selectivity in CO_2 Catalytic Reduction. *J. Am. Chem. Soc.* **140**, 13736–13745 (2018).
12. Matsubu, J. C. *et al.* Adsorbate-mediated strong metal–support interactions in oxide-supported Rh catalysts. *Nature Chem* **9**, 120–127 (2017).
13. Xu, D. *et al.* Advances in higher alcohol synthesis from CO_2 hydrogenation. *Chem* **7**, 849–881 (2021).
14. Kusama, H., Okabe, K., Sayama, K. & Arakawa, H. CO_2 hydrogenation to ethanol over promoted Rh/SiO_2 catalysts. *Catalysis Today* **28**, 261–266 (1996).

15. Zhang, S., Liu, X., Shao, Z., Wang, H. & Sun, Y. Direct CO_2 hydrogenation to ethanol over supported Co_2C catalysts: Studies on support effects and mechanism. *Journal of Catalysis* **382**, 86–96 (2020).
16. Kitamura Bando, K., Soga, K., Kunimori, K. & Arakawa, H. Effect of Li additive on CO_2 hydrogenation reactivity of zeolite supported Rh catalysts. *Applied Catalysis A: General* **175**, 67–81 (1998).
17. Wang, Y. *et al.* Direct Conversion of CO_2 to Ethanol Boosted by Intimacy-Sensitive Multifunctional Catalysts. *ACS Catal.* **11**, 11742–11753 (2021).
18. Goud, D. *et al.* Strain-Enhanced Phase Transformation of Iron Oxide for Higher Alcohol Production from CO_2. *ACS Catal.* **12**, 11118–11128 (2022).
19. Xu, D., Yang, H., Hong, X., Liu, G. & Edman Tsang, S. C. Tandem Catalysis of Direct CO_2 Hydrogenation to Higher Alcohols. *ACS Catal.* **11**, 8978–8984 (2021).
20. Wang, Y., Zhang, X., Hong, X. & Liu, G. Sulfate-Promoted Higher Alcohol Synthesis from CO_2 Hydrogenation. *ACS Sustainable Chem. Eng.* **10**, 8980–8987 (2022).
21. Ding, L. *et al.* CO_2 Hydrogenation to Ethanol over Cu@Na-Beta. *Chem* **6**, 2673–2689 (2020).
22. An, B. *et al.* Cooperative copper centres in a metal–organic framework for selective conversion of CO_2 to ethanol. *Nat Catal* **2**, 709–717 (2019).
23. Wu, Q., Shen, C., Rui, N., Sun, K. & Liu, C. Experimental and theoretical studies of CO_2 hydrogenation to methanol on Ru/In_2O_3. *Journal of CO2 Utilization* **53**, 101720 (2021).
24. Pinheiro Araújo, T. *et al.* Flame Spray Pyrolysis as a Synthesis Platform to Assess Metal Promotion in In_2O_3-Catalyzed CO_2 Hydrogenation. *Advanced Energy Materials* **12**, 2103707 (2022).

25. Frei, M. S. *et al.* Nanostructure of nickel-promoted indium oxide catalysts drives selectivity in CO_2 hydrogenation. *Nat Commun* **12**, 1960 (2021).

26. Geng, F., Zhan, X. & Hicks, J. C. Promoting Methanol Synthesis and Inhibiting CO_2 Methanation with Bimetallic In–Ru Catalysts. *ACS Sustainable Chem. Eng.* **9**, 11891–11902 (2021).

27. Tauster, S. J., Fung, S. C. & Garten, R. L. Strong metal-support interactions. Group 8 noble metals supported on titanium dioxide. *J. Am. Chem. Soc.* **100**, 170–175 (1978).

28. Tauster, S. J. & Fung, S. C. Strong metal-support interactions: Occurrence among the binary oxides of groups II_A–V_B. *Journal of Catalysis* **55**, 29–35 (1978).

29. Tsoukalou, A. *et al.* Structural Evolution and Dynamics of an In_2O_3 Catalyst for CO_2 Hydrogenation to Methanol: An Operando XAS-XRD and In Situ TEM Study. *J. Am. Chem. Soc.* **141**, 13497–13505 (2019).

30. Snider, J. L. *et al.* Revealing the Synergy between Oxide and Alloy Phases on the Performance of Bimetallic In–Pd Catalysts for CO_2 Hydrogenation to Methanol. *ACS Catal.* **9**, 3399–3412 (2019).

31. Wegener, E. C. *et al.* Structure and reactivity of Pt–In intermetallic alloy nanoparticles: Highly selective catalysts for ethane dehydrogenation. *Catalysis Today* **299**, 146–153 (2018).

32. Otsuka, K., Yasui, T. & Morikawa, A. The Decomposition of Water on the CO- or H_2-reduced Indium Oxide. *BCSJ* **55**, 1768–1771 (1982).

33. Stangeland, K., Li, H. & Yu, Z. Thermodynamic Analysis of Chemical and Phase Equilibria in CO_2 Hydrogenation to Methanol, Dimethyl Ether, and Higher Alcohols. *Ind. Eng. Chem. Res.* **57**, 4081–4094 (2018).

34. Riguetto, B. A., Bueno, J. M. C., Petrov, L. & Marques, C. M. P. An infrared study of CO adsorption on silica-supported Ru–Sn catalysts. *Spectrochimica Acta Part A: Molecular and Biomolecular Spectroscopy* **59**, 2141–2150 (2003).

35. Zhou, C. *et al.* Steering CO_2 hydrogenation toward C–C coupling to hydrocarbons using porous organic polymer/metal interfaces. *Proceedings of the National Academy of Sciences* **119**, e2114768119 (2022).

Selective CO_2 Hydrogenation to Ethanol over Ru-In Catalysts

Supplementary Information

1. The choice of first-order model for deactivation analysis

We invoke empirical first-order decay model (Fogler, H. S. (2016). *Catalyst Deactivation*. Elements of chemical reaction engineering.) to describe the catalytic behavior of Ru/In_2O_3-ZrO_2 (CD) catalyst.

$$r_{EtOH}(t) = e^{-k_{EtOH} \cdot t}$$

Where r_{EtOH} represents the catalytic activity of the catalyst (time-dependent) and k_{EtOH} represents the empirical deactivation rate constant.

We hypothesize that the ethanol producing sites were converted to methanol-producing sites. As a result, methanol production rate should be increasing with time, simultaneous to the decrease of ethanol production:

$$r_{MeOH}(t) = r_{MeOH}(\infty) \; - \; e^{-k_{MeOH} \cdot t}$$

Where r_{MeOH} represents the catalytic activity of the catalyst (time-dependent) and k_{MeOH} represents the empirical activation rate constant. $r_{MeOH}(\infty)$ represents the methanol production rate at steady state when all ethanol producing sites have converted.

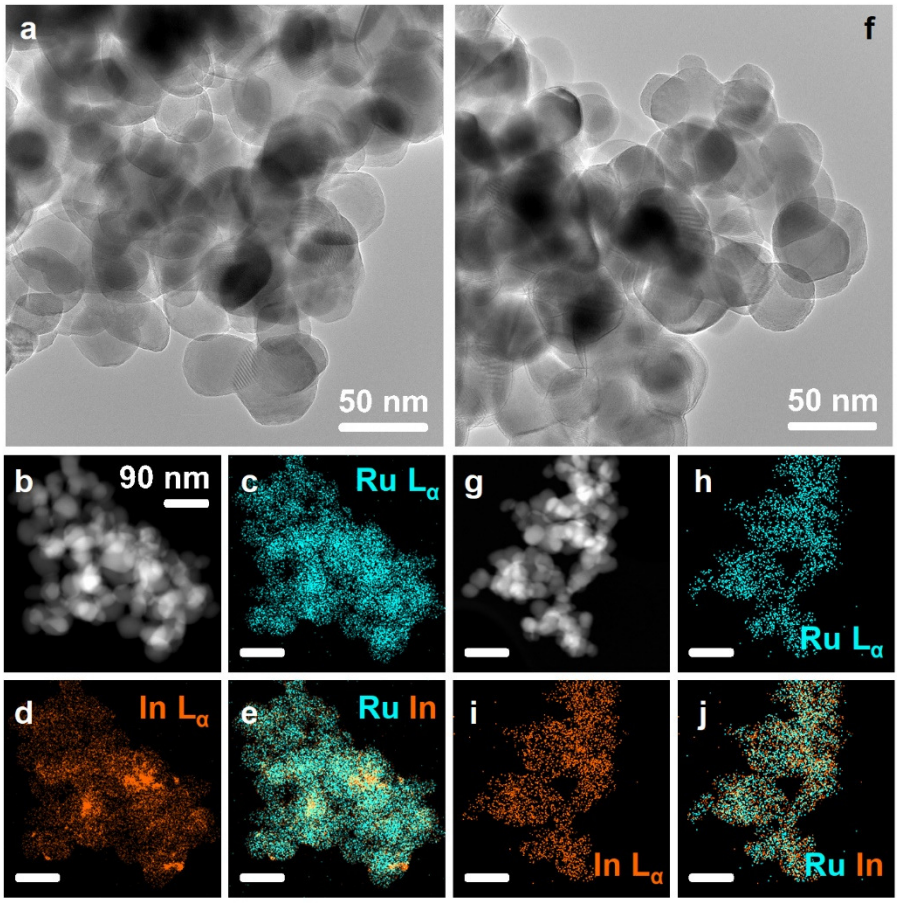

Fig. S1: TEM and STEM-EDS characterizations of Ru/In_2O_3-ZrO_2 (IWI) catalyst at different stages of reaction. **a,f** Representative TEM images, **b-e,g-j** Ru L_α and In L_α EDS maps of Ru/In_2O_3-ZrO_2 (IWI) catalyst after (**a-e**) 0 minute and (**f-j**) 180 minutes of reaction. All scale bars in **b-e,g-j** are 90 nm.

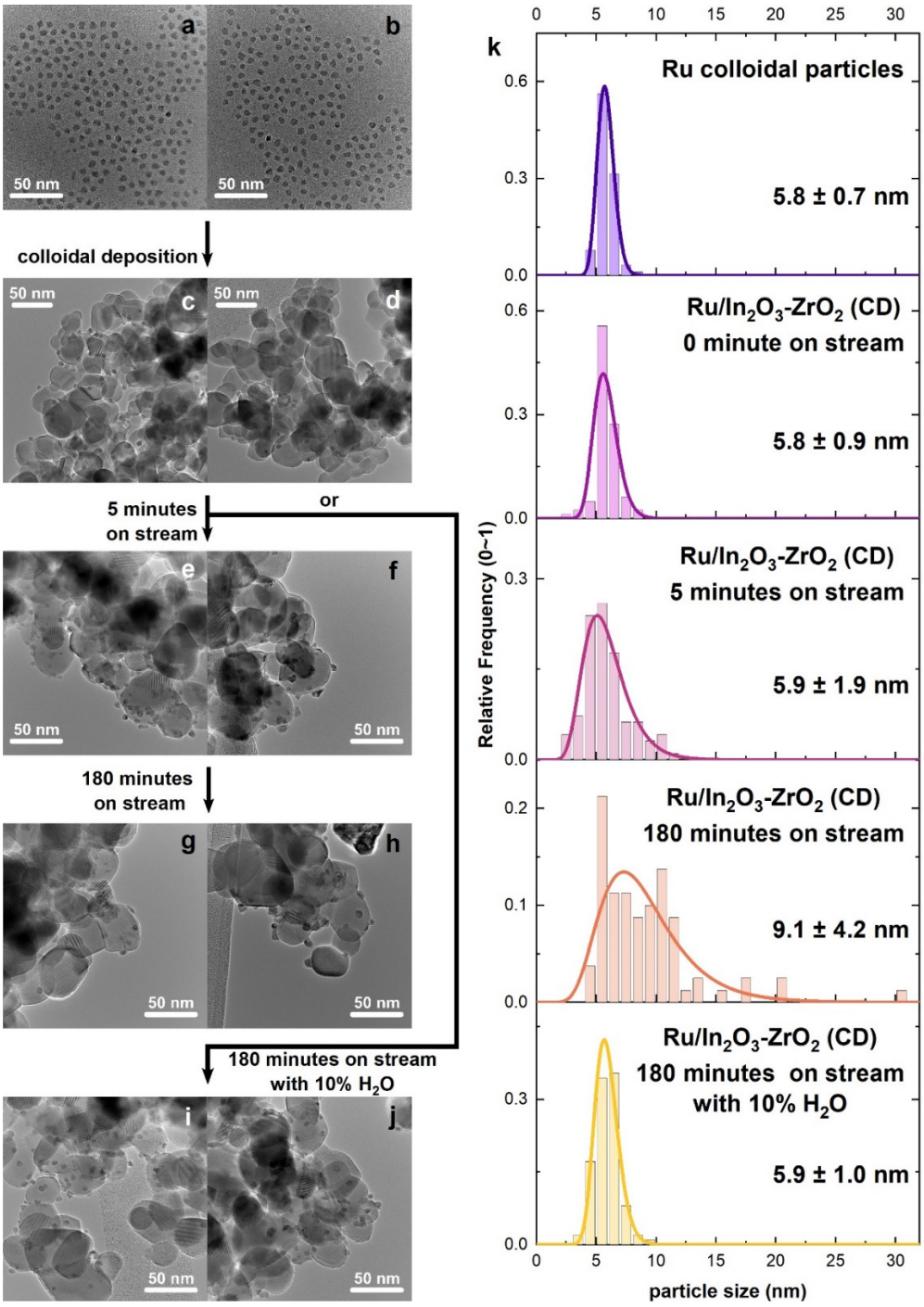

Fig. S2 TEM images of **a,b** Ru colloidal nanoparticles; **c,d** as-synthesized Ru/In_2O_3-ZrO_2 (CD) catalyst; **e,f** Ru/In_2O_3-ZrO_2 (CD) catalyst after 5 minutes on stream; **g,h** Ru/In_2O_3-ZrO_2 (CD) catalyst after 180 minutes on stream; **i,j** Ru/In_2O_3-ZrO_2 (CD) catalyst after 180 minutes on stream with 10% additional H_2O. **k** histograms of Ru particle size (~100 particles each sample) with log-normal distribution curves.

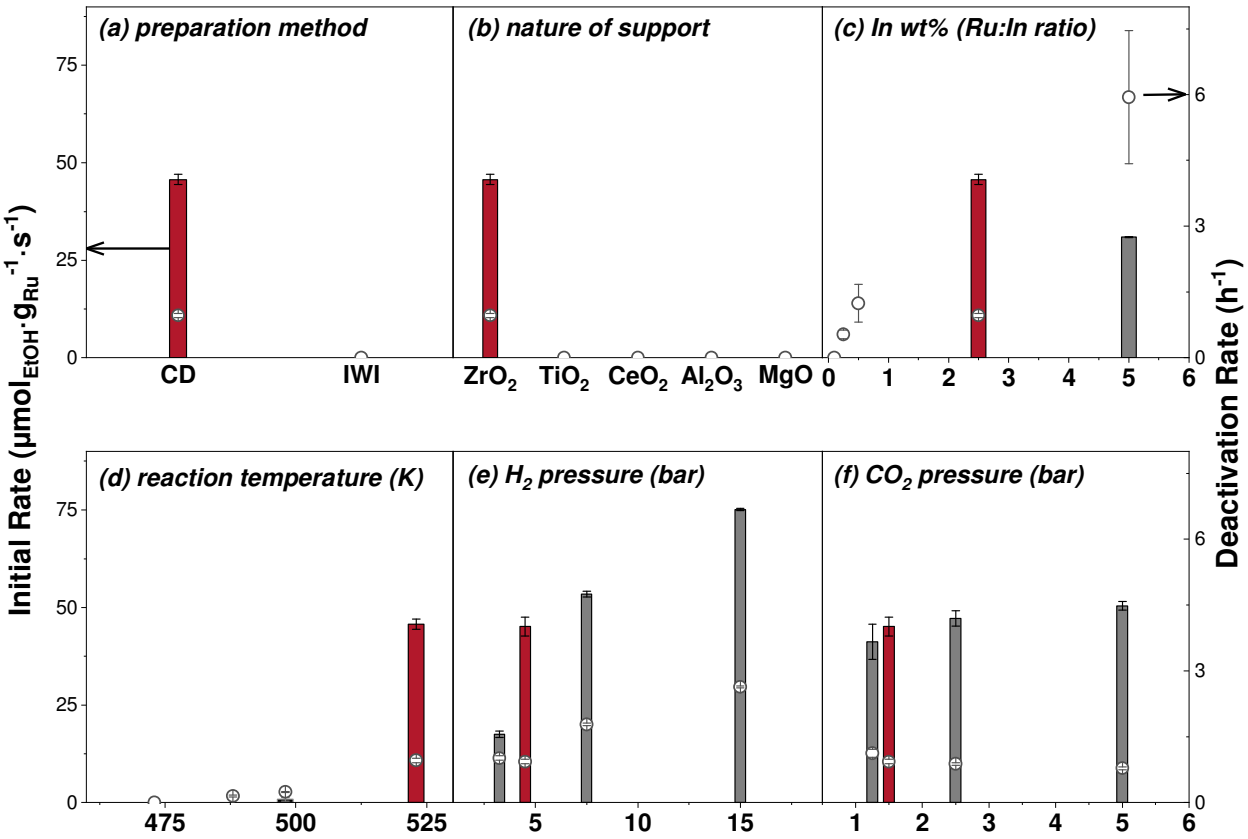

Fig. S3 The effect of **a** preparation method, **b** choice of support, **c** Ru:In ratio, **d** reaction temperature, **e** H_2 partial pressure and **f** CO_2 partial pressure on the initial ethanol production rate (columns, left axis) and catalyst deactivation rate (points, right axis). The catalyst was colloidally prepared Ru/In_2O_3-ZrO_2 unless noted otherwise. Ru weight loading was kept constant at 0.5 wt% while In remained as 2.5 wt% except in **c** where exact indium loading was given. Initial ethanol production rate and catalyst deactivation rate obtained at 523 K, 6 bar, 30 ml·min^{-1} of 3:1 H_2:CO_2 was used as benchmarks which are highlighted in red.

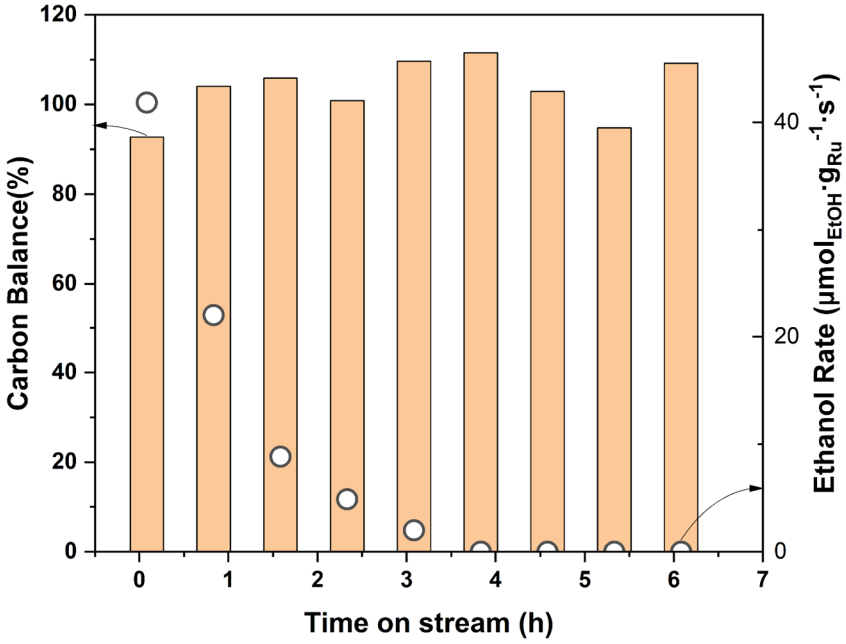

Fig. S4: Carbon balance and ethanol production rates as functions of time on stream. Carbon balance (columns, left axis) are defined as amount of product produced/amount of CO_2 consumed. Data shown in this figure corresponds to the experiment described in Fig 1a, which is colloidally deposited (CD) Ru/In_2O_3-ZrO_2 catalysts tested at 523 K, 6 bar, 30 ml·min^{-1} of 3:1 H_2:CO_2. Ethanol production rates were replotted from Fig 1b. It can be seen that no obvious correlation between carbon balance and ethanol deactivation rates are established.

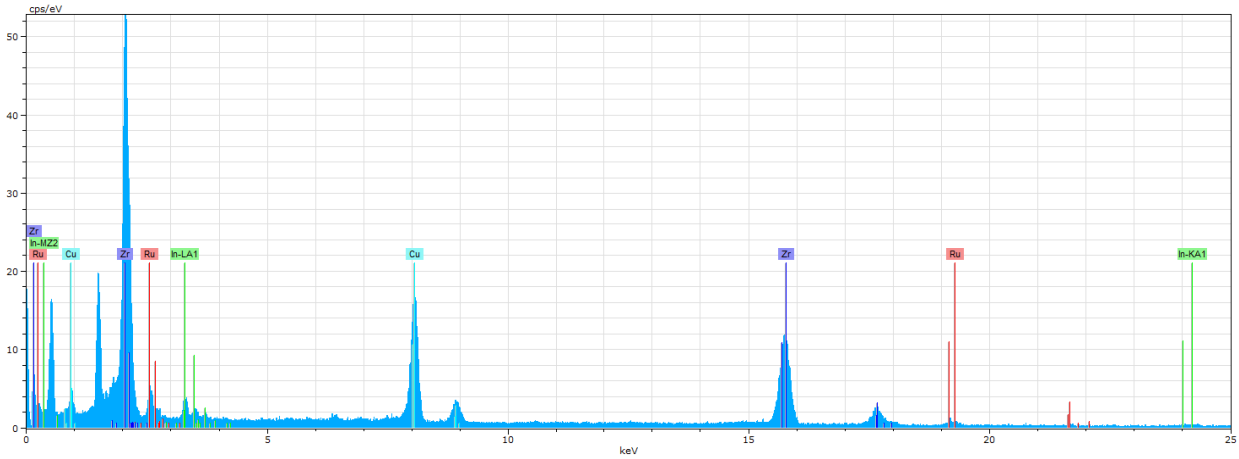

Fig. S5: Representative EDS spectrum of summed pixels in EDS maps. Specifically, this spectrum is from the EDS map shown in Fig 2n-p. Characteristic peaks for Ru, In, Zr and Cu (from TEM grid) are labeled.

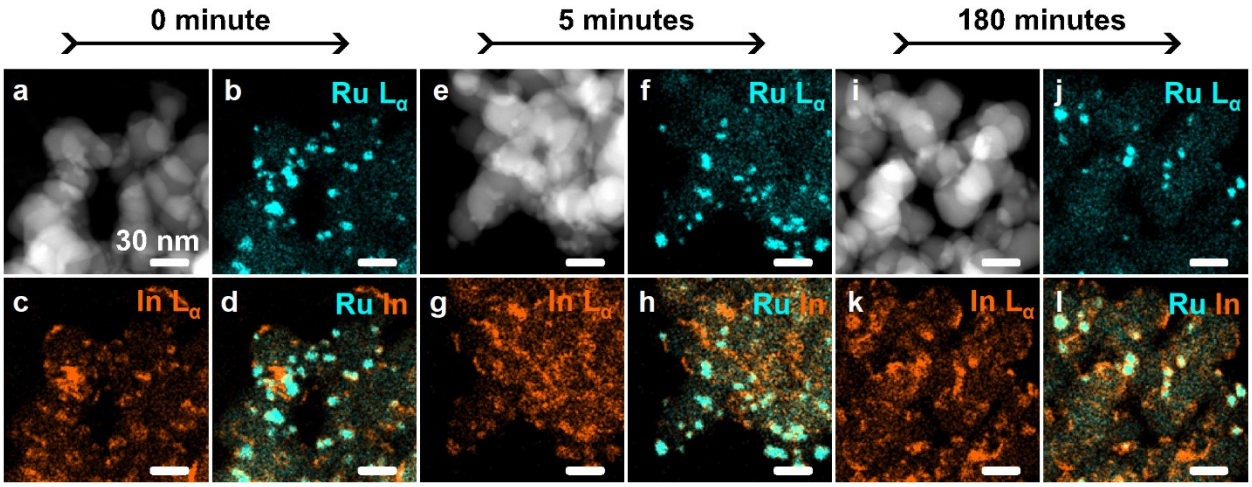

Fig. S6: Additional STEM-EDS characterizations of Ru/In_2O_3-ZrO_2 (CD) catalyst at different stages of reaction. **a,e,i** Representative STEM images, **b-d**,**f-h**,**j-l** Ru L_α and In L_α EDS maps of Ru/In_2O_3-ZrO_2 (CD) catalyst after (**a-d**) 0 minute, (**e-h**) 5 minutes and (**i-l**) 180 minutes of reaction.

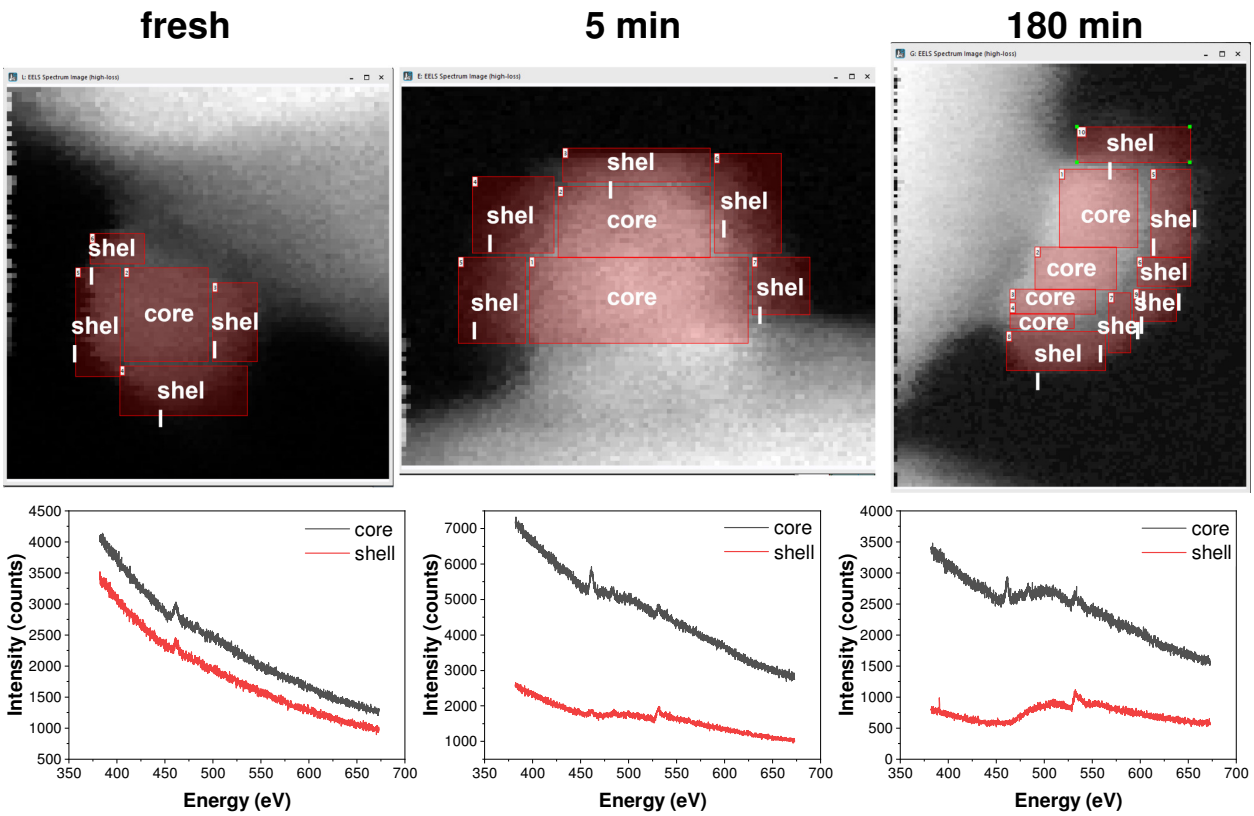

Fig. S7: Additional information on EELS analysis from Ru/In_2O_3-ZrO_2 (CD) catalyst at different stages of reaction, corresponding to Fig 2f, l and r. Guided by the contrast differences, EELS maps were divided into many regions defined as shells (low contrast, usually within 1 nm depth from surface) and cores (high contrast). EELS signal from cores and shells were then summed and background removed, respectively. The raw spectra without background removal were also plotted here for clarity.

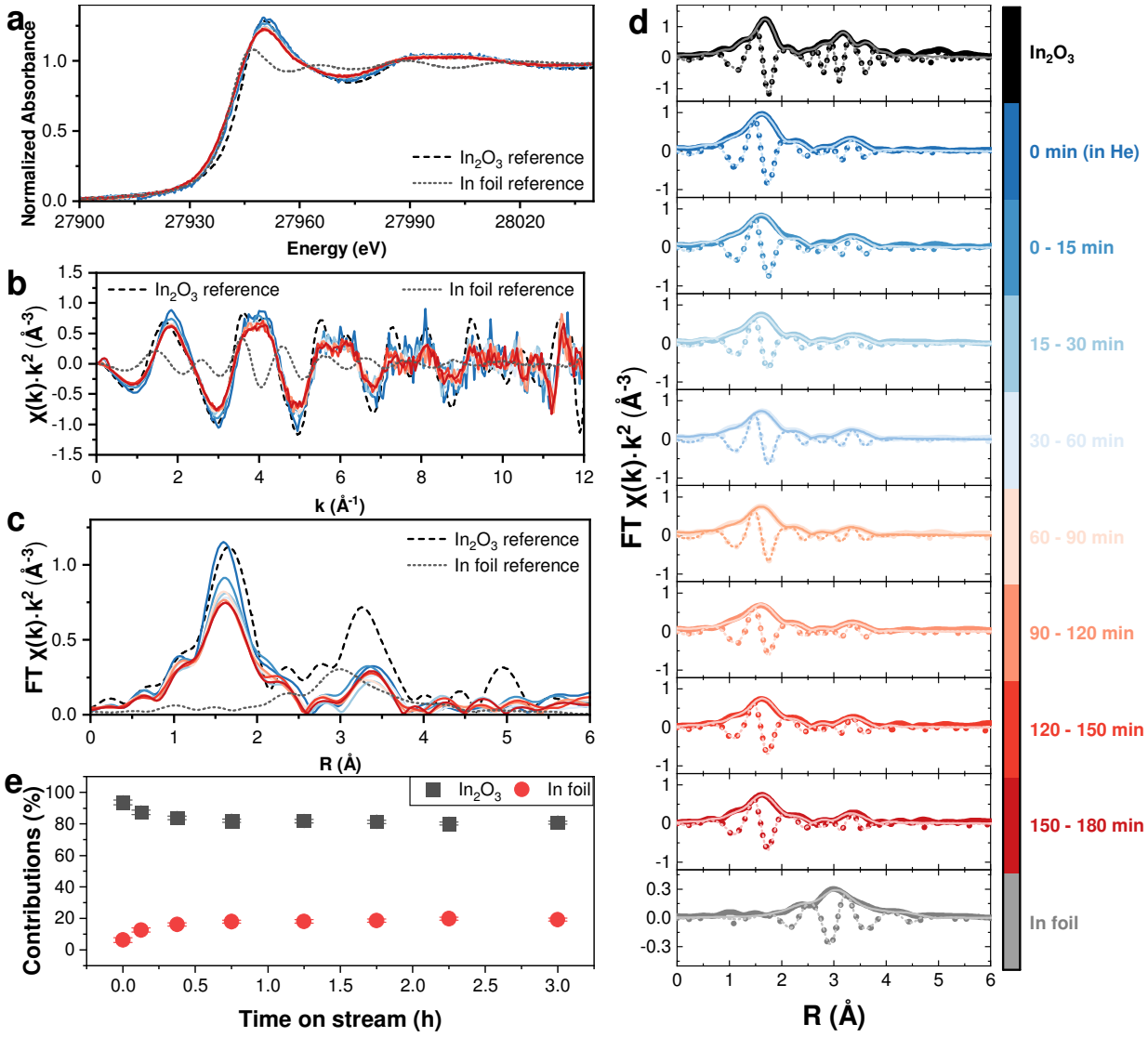

Fig. S8: *operando* In K-edge XAS of Ru/In_2O_3-ZrO_2 during CO_2 hydrogenation at 523 K, 6 bar, 20 ml·min^{-1} of 3:1 H_2:CO_2 **a** In K-edge XANES spectra, **b** k^2-weighted In K-edge EXAFS spectra and **c** In K-edge EXAFS spectra of In_2O_3 powder (dash, as reference), In foil (dot, as reference) and Ru/In_2O_3-ZrO_2 at different stages of reaction. XAS data was continuously collected and merged into different groups. Spectra in **d** are individual plots of the EXAFS spectra in **c** together with the fits. Thick light traces are experimental data; Dark thinner traces are fits; solid traces are magnitudes; dotted traces are imaginary components of the Fourier transform. **a-e** share same legends, which are shown as color scales on the right. **e** Linear combination fitting results of In K-edge XANES from Ru/In_2O_3-ZrO_2 at different stages of reaction. In foil and In_2O_3 powder are used as references.

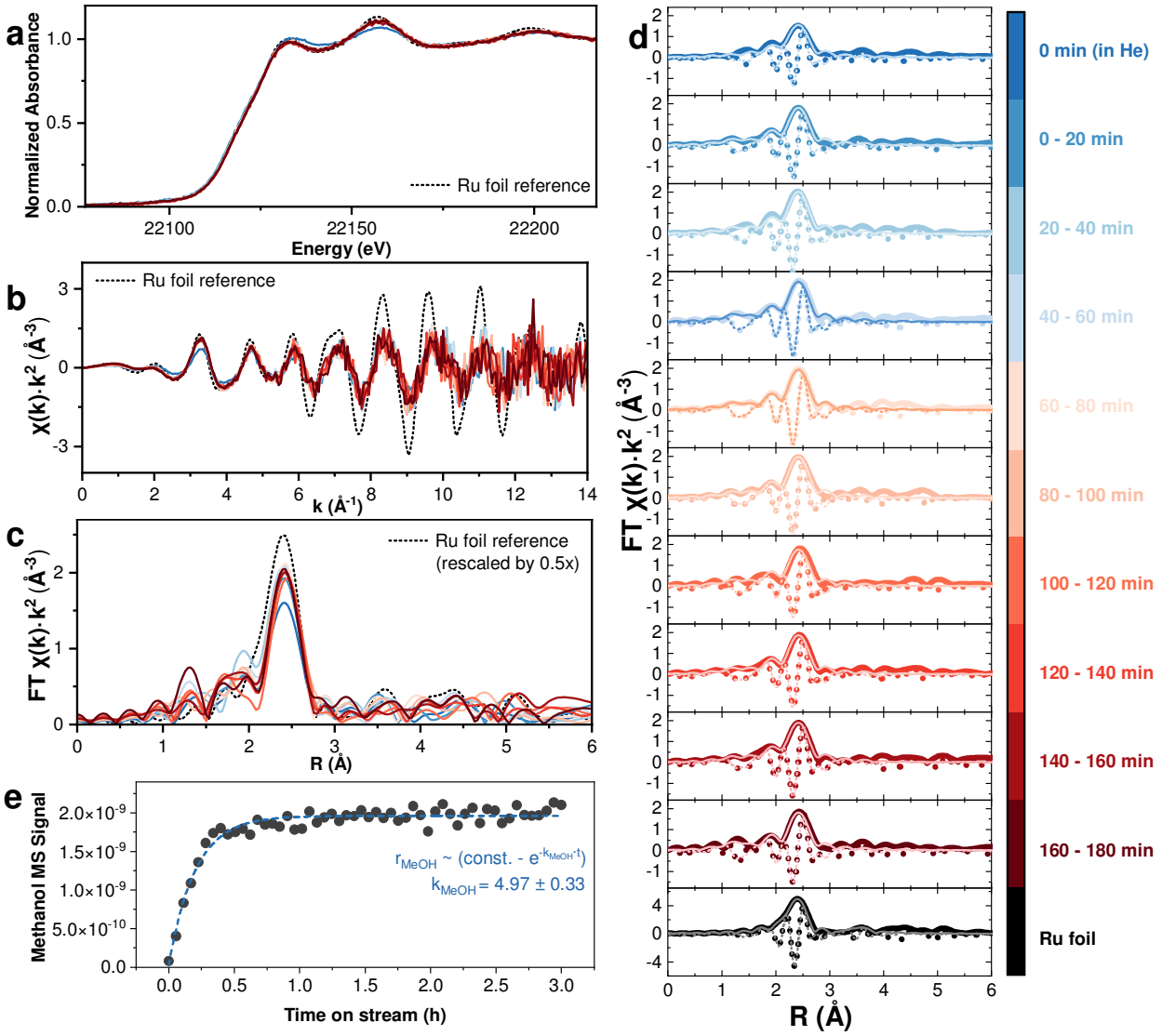

Fig. S9: *operando* Ru K-edge XAS of Ru/In_2O_3-ZrO_2 during CO_2 hydrogenation at 523 K, 6 bar, 20 ml·min^{-1} of 3:1 H_2:CO_2 **a** Ru K-edge XANES spectra, **b** k^2-weighted Ru K-edge EXAFS spectra and **c** Ru K-edge EXAFS spectra of Ru foil (dot, as reference) and Ru/In_2O_3-ZrO_2 at different stages of reaction. XAS data was continuously collected and merged into different groups. Spectra in **d** are individual plots of the EXAFS spectra in **c** together with the fits. Thick light traces are experimental data; Dark thinner traces are fits; solid traces are magnitudes; dotted traces are imaginary components of the Fourier transform. **a-d** share same legends, which are shown as color scales on the right. **e** Methanol (M/Z=31) signal from online mass-spectrometer analysis as a function of time. Dotted line is the fit of methanol signal using self-limiting first order growth model and k_{MeOH} is the kinetic rate constant. Note that ethanol (M/Z=45 or 46) was below detection limit due to overlap with CO_2 isotopes such as $^{13}CO_2$ and $C^{16}O^{17}O$.

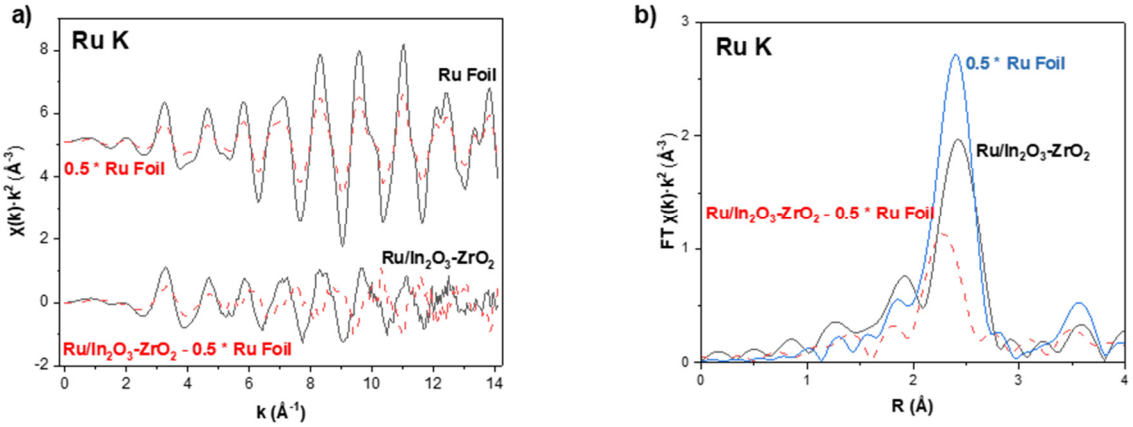

Fig. S10: Identification of Ru-In scattering paths. Given the similarities in atomic radius, Ru-Ru paths and Ru-In paths require caution to distinguish. We first examined whether there were notable differences between the Ru foil and Ru/In_2O_3-ZrO_2 EXAFS. Shown in **a**, the two spectra (shown in black) indeed possessed very similar features, such as the frequency and amplitude of oscillations. However, small but non-trivial differences can be revealed when a difference spectrum (dashed red traces) is taken by subtracting the Ru foil spectrum from the Ru/In_2O_3-ZrO_2 spectrum at a weight of 0.5. A similar "difference" spectrum of the Ru foil itself was also produced as a reference. It can be clearly seen that there existed a contribution to the Ru/In_2O_3-ZrO_2 spectrum that was in a notably different phase. Upon fourier transformation (dashed red trace in panel **b**), it can be clearly seen that the difference between Ru/In_2O_3-ZrO_2 and Ru foil can be ascribed to a shell that has similar but shorter distance than Ru-Ru, which we hypothesize to be Ru-In, given that it would have been too long for Ru-O but too short to be plausible for Ru-Zr.

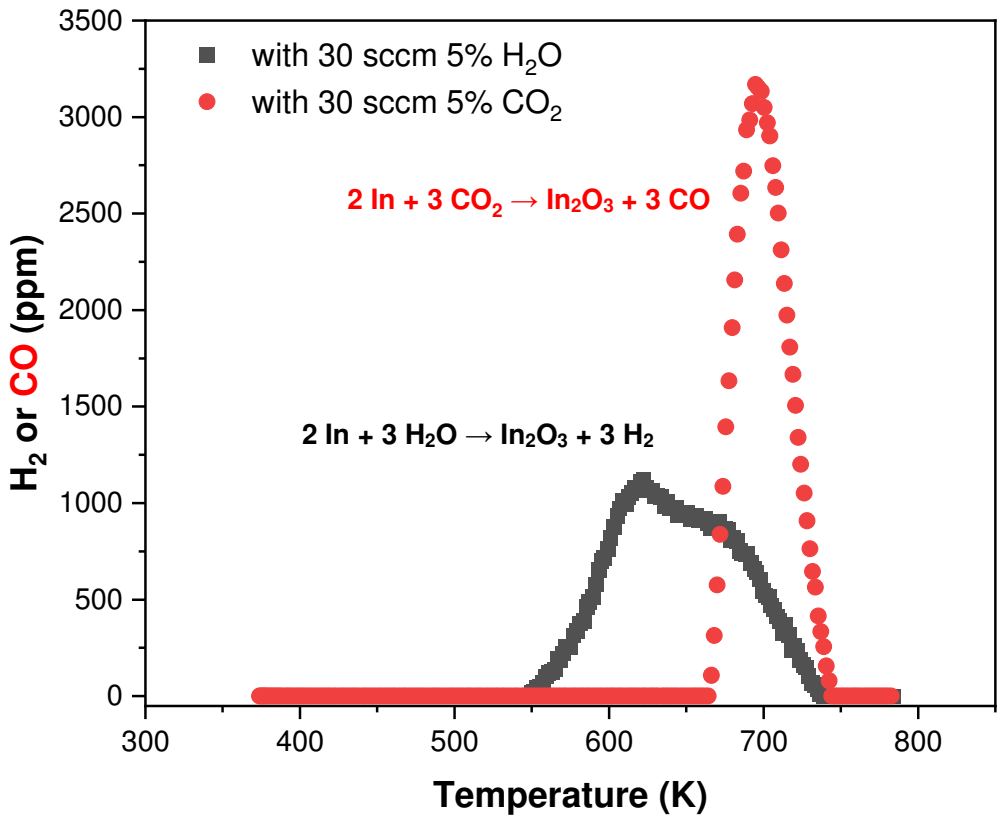

Fig. S11 Catalyst regeneration (temperature programmed oxidation) with steam or CO_2. Ru/In_2O_3-ZrO_2 catalysts were intentionally deactivated by H_2 reduction at 673 K for 1 hour before being exposed to oxidants. The production of hydrogen (from reduction of water) or CO (from reduction of CO_2) were lotted as the indicator of catalyst regeneration. Although CO_2 did also oxidize indium (as evidenced by the production of CO), the oxidation occurred at a much higher temperature (660 K) than with steam as the oxidant (550 K). Therefore, water is a stronger oxidizer than CO_2 (as is known from steam reforming catalysis).

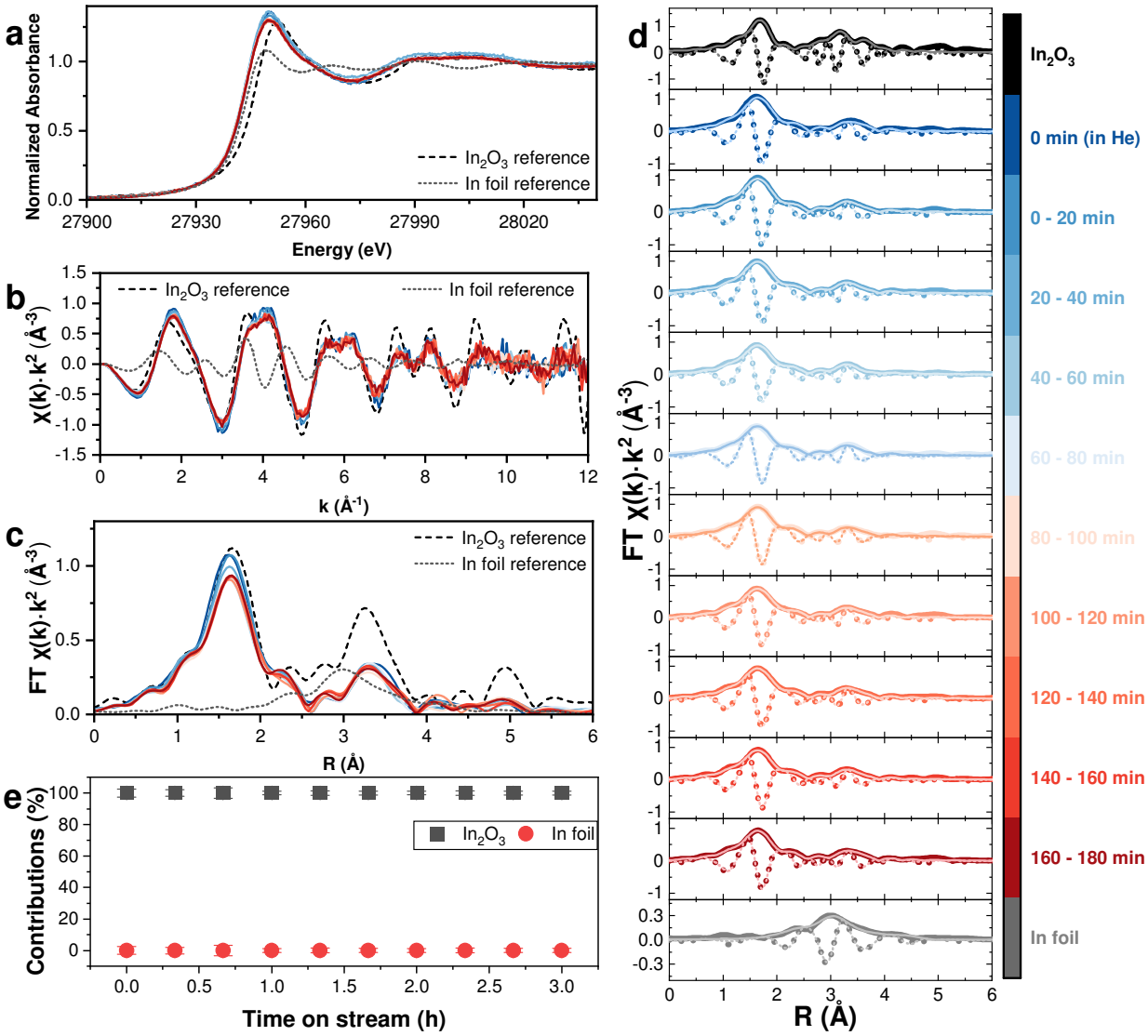

Fig. S12: *operando* In K-edge XAS of Ru/In_2O_3-ZrO_2 during CO_2 hydrogenation at 498 K, 6 bar, 20 ml·min^{-1} of 3:1 H_2:CO_2 and 10% added steam **a** In K-edge XANES spectra, **b** k^2-weighted In K-edge EXAFS spectra and **c** In K-edge EXAFS spectra of In_2O_3 powder (dash, as reference), In foil (dot, as reference) and Ru/In_2O_3-ZrO_2 at different stages of reaction. XAS data was continuously collected and merged into different groups. Spectra in **d** are individual plots of the EXAFS spectra in **c** together with the fits. Thick light traces are experimental data; Dark thinner traces are fits; solid traces are magnitudes; dotted traces are imaginary components of the Fourier transform. **a-e** share same legends, which are shown as color scales on the right. **e** Linear combination fitting results of In K-edge XANES from Ru/In_2O_3-ZrO_2 at different stages of reaction. In foil and In_2O_3 powder are used as references.

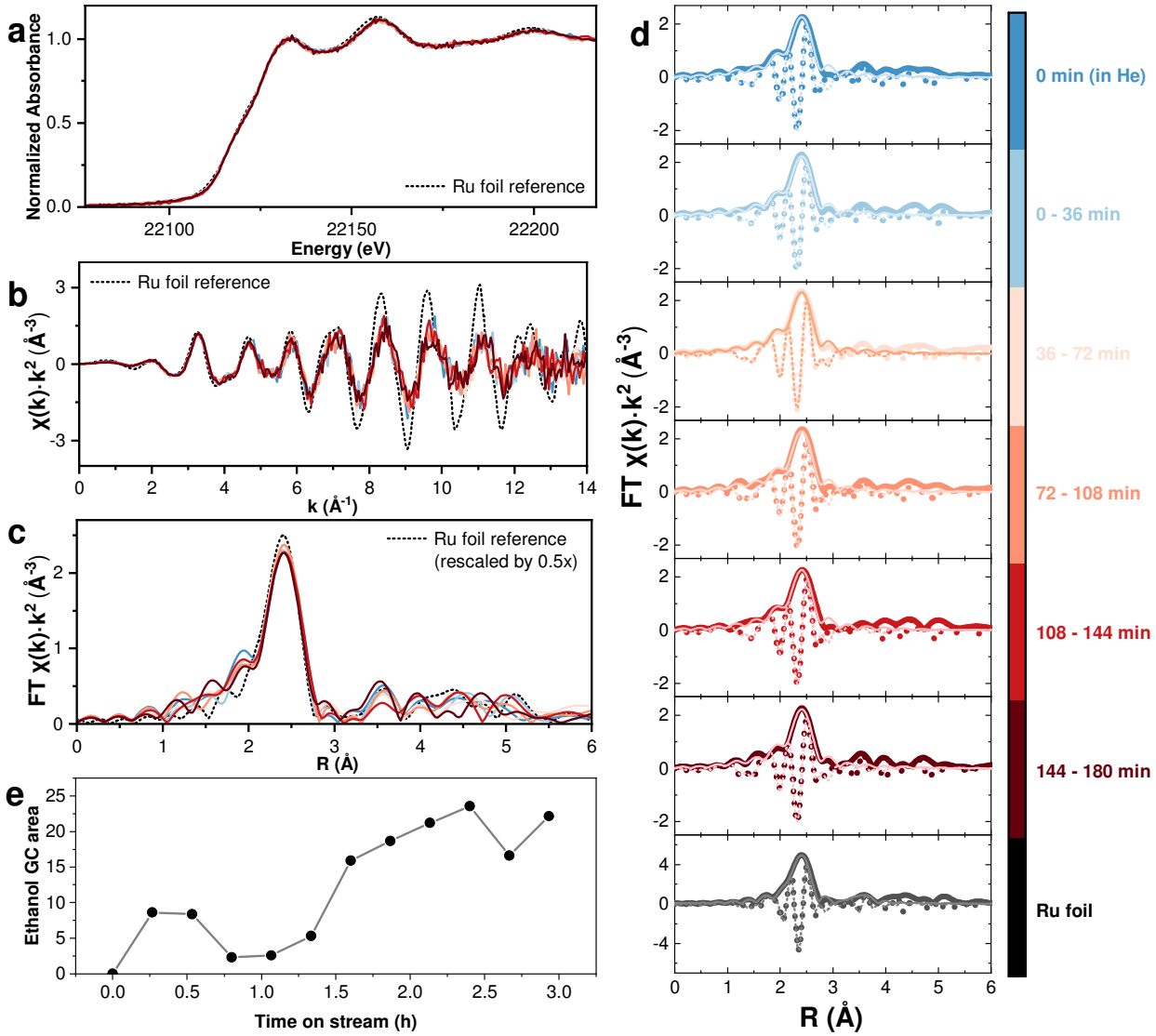

Fig. S13: *operando* Ru K-edge XAS of Ru/In_2O_3-ZrO_2 during CO_2 hydrogenation at 498 K, 6 bar, 20 ml·min^{-1} of 3:1 H_2:CO_2 and 10% added steam **a** Ru K-edge XANES spectra, **b** k^2-weighted Ru K-edge EXAFS spectra and **c** Ru K-edge EXAFS spectra of Ru foil (dot, as reference) and Ru/In_2O_3-ZrO_2 at different stages of reaction. XAS data was continuously collected and merged into different groups. Spectra in **d** are individual plots of the EXAFS spectra in **c** together with the fits. Thick light traces are experimental data; Dark thinner traces are fits; solid traces are magnitudes; dotted traces are imaginary components of the Fourier transform. **a-d** share same legends, which are shown as color scales on the right. **e** Ethanol area from online gas chromatography analysis as a function of time.

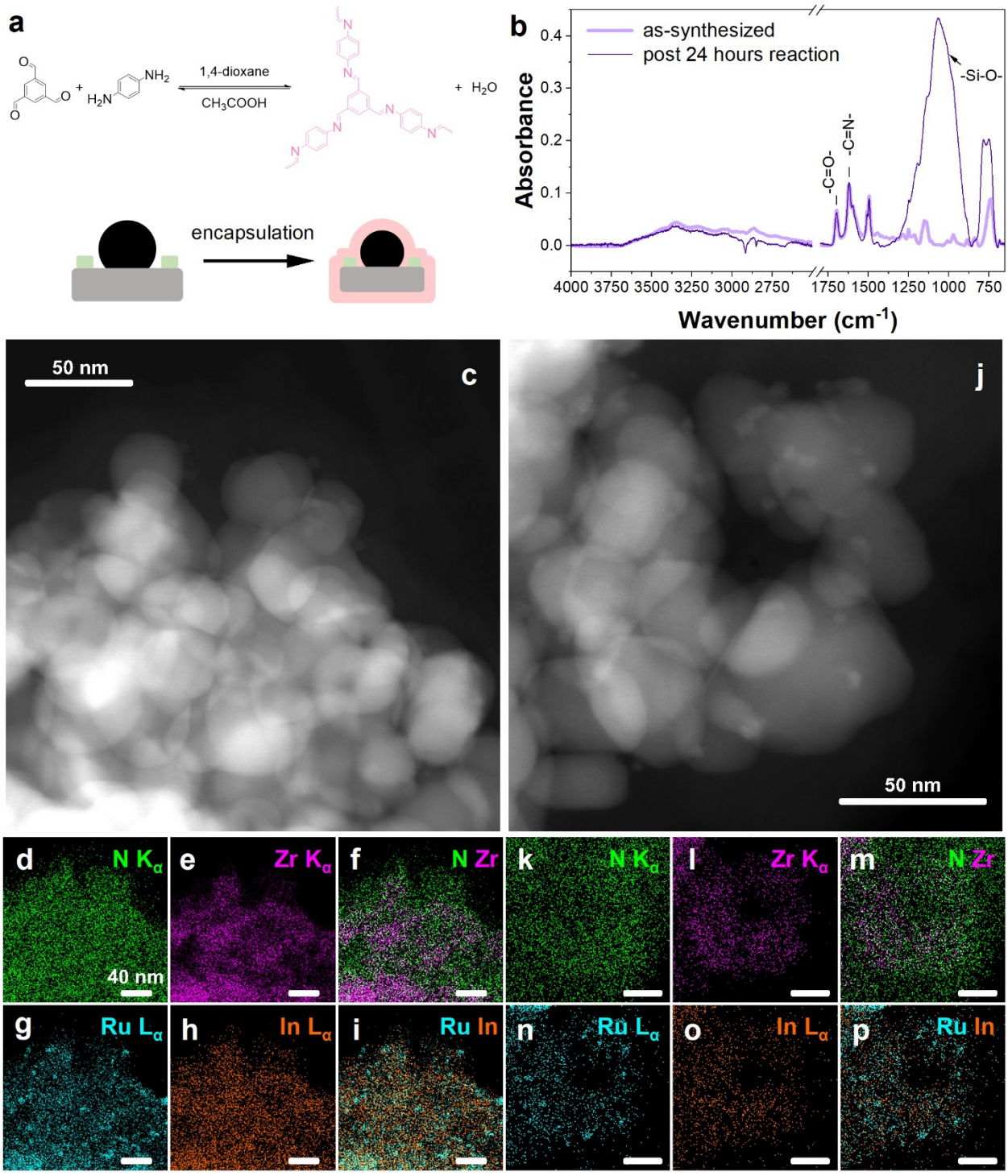

Fig. S14: Additional characterizations of IPOP/Ru/In_2O_3-ZrO_2 (CD) catalyst at different stages of reaction. **a** Schematic of the encapsulation procedure. Ru/In_2O_3-ZrO_2 is used as substrate, on which an imine-linked polymer is grown, from the condensation reaction between benzene-1,3,5-tricarboxaldehyde and p-phenylenediamine. **b** ATR-IR spectra of the IPOP/Ru/In_2O_3-ZrO_2 (CD) catalyst as synthesized (thick light trace) and after 24 hours of reaction at 498 K, 6 bar, 20 ml·min^{-1} of 3:1 H_2:CO_2 and 10% added steam. IR vibrations related to Si-O species found in the post-test

sample are due to the presence of SiO_2 diluent mixed with the catalyst. **c,j** Representative STEM images, **d-i**,**k-p** N K_α, Zr K_α, Ru L_α and In L_α EDS maps of IPOP/Ru/In_2O_3-ZrO_2 (CD) catalyst (**c-i**) as-synthesized and (**j-p**) after 24 hours of reaction at 498 K, 6 bar, 20 ml·min^{-1} of 3:1 H_2:CO_2 and 10% added steam.

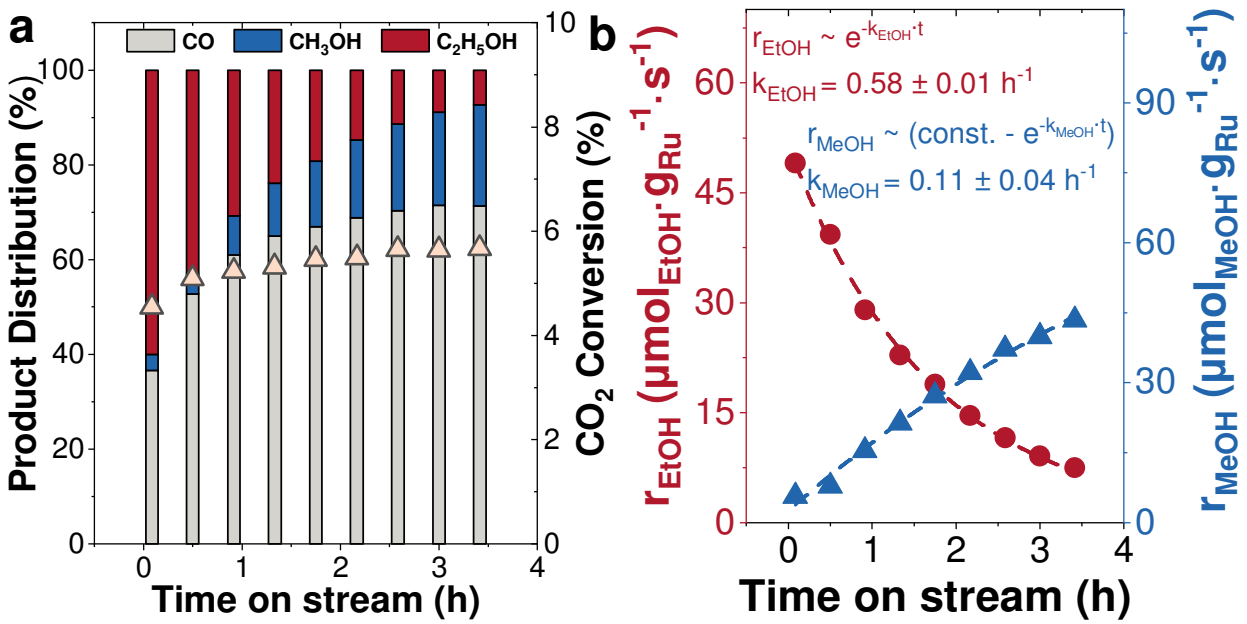

Fig. S15 The effect of polymer encapsulation. a CO_2 conversion and product selectivity and **b** Ethanol production rate of IPOP/Ru/In_2O_3-ZrO_2 catalysts as a function of time on stream at 523 K, 6 bar, 30 ml·min^{-1} of 3:1 H_2:CO_2. Note that the encapsulation by IPOP notably stabilized ethanol production and decreased catalyst deactivation rate from 0.96 h^{-1} to 0.38 h^{-1}.

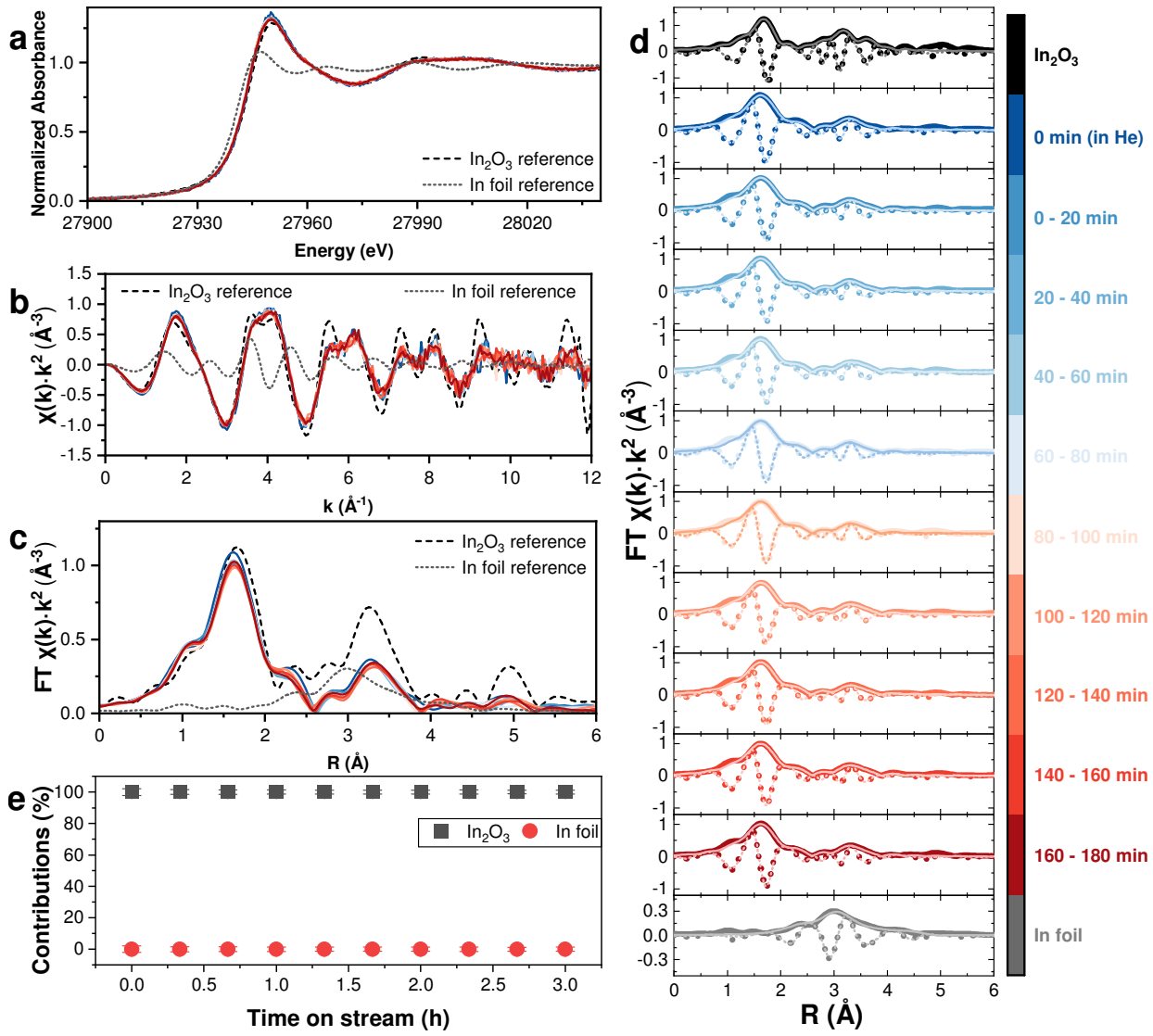

Fig. S16: *operando* In K-edge XAS of IPOP/Ru/In_2O_3-ZrO_2 during CO_2 hydrogenation at 498 K, 6 bar, 20 ml·min^{-1} of 3:1 H_2:CO_2 and 10% added steam **a** In K-edge XANES spectra, **b** k^2-weighted In K-edge EXAFS spectra and **c** In K-edge EXAFS spectra of In_2O_3 powder (dash, as reference), In foil (dot, as reference) and IPOP/Ru/In_2O_3-ZrO_2 at different stages of reaction. XAS data was continuously collected and merged into different groups. Spectra in **d** are individual plots of the EXAFS spectra in **c** together with the fits. Thick light traces are experimental data; Dark thinner traces are fits; solid traces are magnitudes; dotted traces are imaginary components of the Fourier transform. **a-e** share same legends, which are shown as color scales on the right. **e** Linear combination fitting results of In K-edge XANES from IPOP/Ru/In_2O_3-ZrO_2 at different stages of reaction. In foil and In_2O_3 powder are used as references.

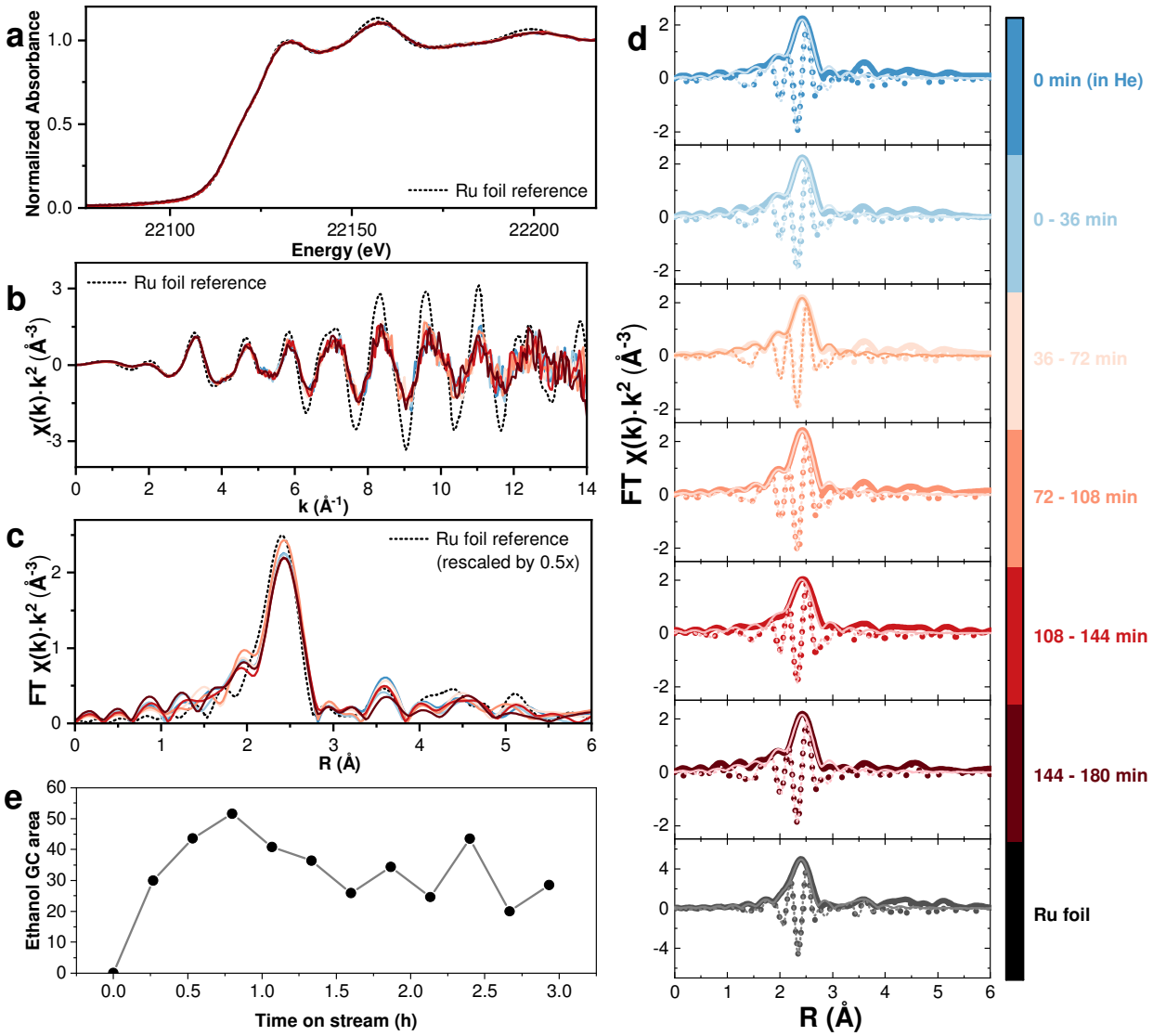

Fig. S17: *operando* Ru K-edge XAS of IPOP/Ru/In_2O_3-ZrO_2 during CO_2 hydrogenation at 498 K, 6 bar, 20 ml·min^{-1} of 3:1 H_2:CO_2 and 10% added steam **a** Ru K-edge XANES spectra, **b** k^2-weighted Ru K-edge EXAFS spectra and **c** Ru K-edge EXAFS spectra of Ru foil (dot, as reference) and IPOP/Ru/In_2O_3-ZrO_2 at different stages of reaction. XAS data was continuously collected and merged into different groups. Spectra in **d** are individual plots of the EXAFS spectra in **c** together with the fits. Thick light traces are experimental data; Dark thinner traces are fits; solid traces are magnitudes; dotted traces are imaginary components of the Fourier transform. **a-d** share same legends, which are shown as color scales on the right. **e** Ethanol area from online gas chromatography analysis as a function of time.

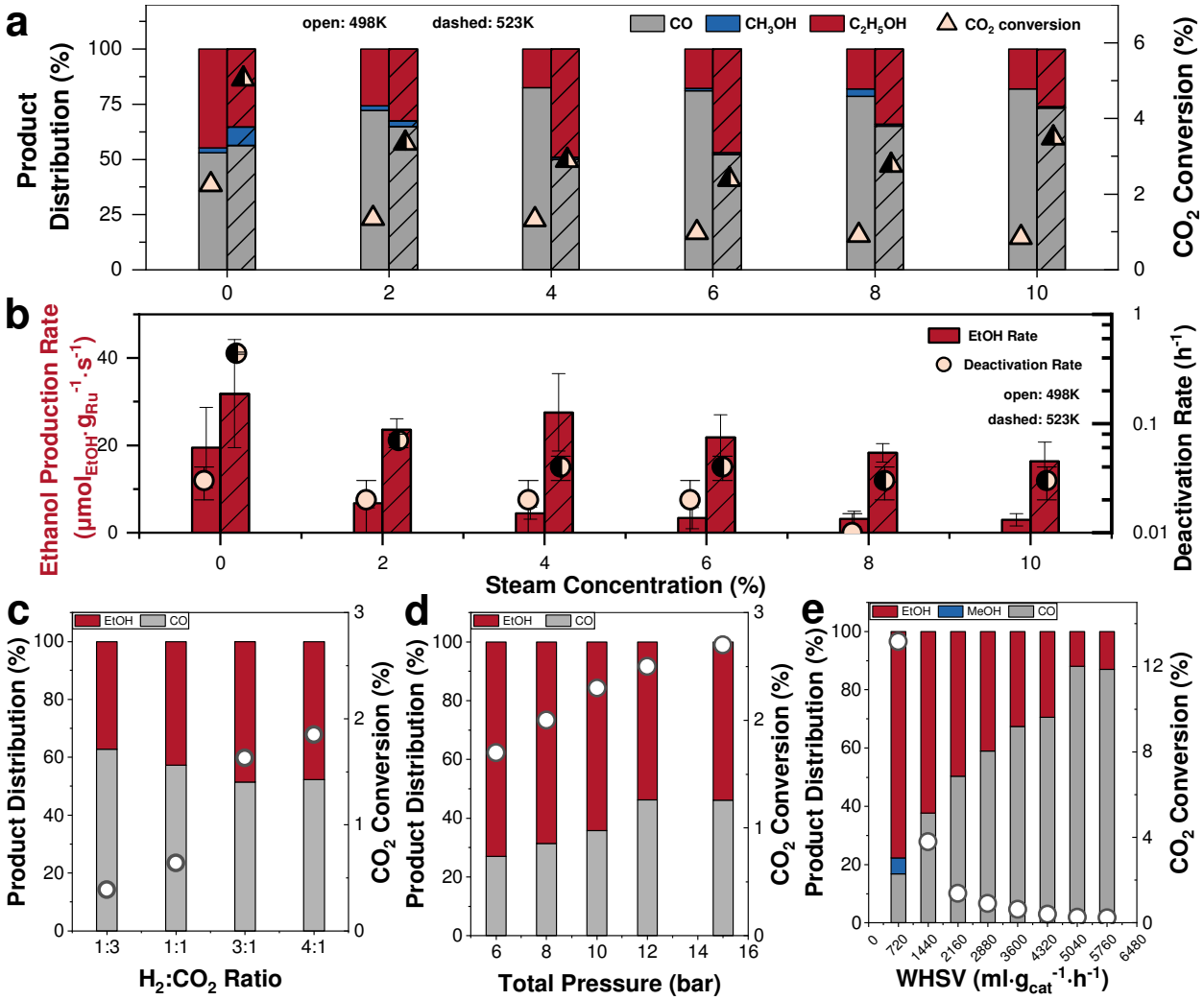

Fig. S18 The effect of temperature, steam concentration, total pressure, H_2:CO_2 ratio and WHSV on IPOP/Ru/In_2O_3-ZrO_2. (a,b) Effect of reaction temperature and steam concentration on (a) product distribution and CO_2 conversion and (b) ethanol production rate and catalyst deactivation rate. WHSV = 5143 ml·g_{cat}^{-1}·h^{-1} and total pressure = 6 bar. (c) Effect of reactant ratio. Reaction temperature = 498 K, WHSV = 3600 ml·g_{cat}^{-1}·h^{-1} and total pressure = 6 bar. H_2:H_2O ratio was kept at 6.75:1. (d) Effect of total pressure. Reaction temperature = 498 K, WHSV = 3600 ml·g_{cat}^{-1}·h^{-1}. H_2, CO_2 and H_2O concentrations were 67.5%, 22.5% and 10%, respectively. (e) Effect of WHSV. Reaction temperature = 498 K, total pressure = 15 bar. H_2, CO_2 and H_2O concentrations were 67.5%, 22.5% and 10%, respectively.

TOS (min)	Path	R (Å)	σ^2(Å)	CN	
0	In-O	2.15 ± 0.00	0.011 ± 0.001	6.02 ± 0.32	
	In-In (1)	3.38 ± 0.00	0.008 ± 0.001	3.03± 0.63	4.22 ± 1.32
	In-In (2)	3.85 ± 0.00	0.004 ± 0.003	1.19 ± 0.69	
	In-Ru	2.62 ± 0.01	0.006 (set)	0.13 ± 0.21	
0-15	In-O	2.15 ± 0.00	0.011 ± 0.001	5.27 ± 0.26	
	In-In (1)	3.38 ± 0.00	0.008 ± 0.001	2.87 ± 0.52	3.59 ± 1.00
	In-In (2)	3.85 ± 0.00	0.004 ± 0.003	0.72 ± 0.48	
	In-Ru	2.62 ± 0.01	0.006 (set)	0.23 ± 0.17	
15-30	In-O	2.15 ± 0.00	0.011 ± 0.001	4.62 ± 0.23	
	In-In (1)	3.38 ± 0.00	0.008 ± 0.001	2.00 ± 0.44	2.73 ± 0.90
	In-In (2)	3.85 ± 0.00	0.004 ± 0.003	0.73 ± 0.46	
	In-Ru	2.62 ± 0.01	0.006 (set)	0.08 ± 0.15	
30-60	In-O	2.15 ± 0.00	0.011 ± 0.001	4.66 ± 0.18	
	In-In (1)	3.38 ± 0.00	0.008 ± 0.001	2.58 ± 0.37	3.66 ± 0.86
	In-In (2)	3.85 ± 0.00	0.004 ± 0.003	1.08 ± 0.49	
	In-Ru	2.62 ± 0.01	0.006 (set)	0.28 ± 0.10	
60-90	In-O	2.15 ± 0.00	0.011 ± 0.001	4.72 ± 0.20	
	In-In (1)	3.38 ± 0.00	0.008 ± 0.001	2.46 ± 0.40	3.11 ± 0.77
	In-In (2)	3.85 ± 0.00	0.004 ± 0.003	0.65 ± 0.37	
	In-Ru	2.62 ± 0.01	0.006 (set)	0.18 ± 0.12	
90-120	In-O	2.15 ± 0.00	0.011 ± 0.001	4.55 ± 0.19	
	In-In (1)	3.38 ± 0.00	0.008 ± 0.001	2.49 ± 0.38	3.38 ± 0.82
	In-In (2)	3.85 ± 0.00	0.004 ± 0.003	0.89 ± 0.44	
	In-Ru	2.62 ± 0.01	0.006 (set)	0.26 ± 0.11	
120-150	In-O	2.15 ± 0.00	0.011 ± 0.001	4.49 ± 0.19	
	In-In (1)	3.38 ± 0.00	0.008 ± 0.001	2.54 ± 0.39	3.42 ± 0.82
	In-In (2)	3.85 ± 0.00	0.004 ± 0.003	0.88 ± 0.43	
	In-Ru	2.62 ± 0.01	0.006 (set)	0.23 ± 0.11	
150-180	In-O	2.15 ± 0.00	0.011 ± 0.001	4.41 ± 0.18	
	In-In (1)	3.38 ± 0.00	0.008 ± 0.001	2.57 ± 0.38	3.40 ± 0.79
	In-In (2)	3.85 ± 0.00	0.004 ± 0.003	0.83 ± 0.41	
	In-Ru	2.62 ± 0.01	0.006 (set)	0.15 ± 0.11	

Table S1: In K-edge EXAFS fitting results of Ru/In_2O_3-ZrO_2 during CO_2 hydrogenation at 523 K, 6 bar, 20 ml·min^{-1} of 3:1 H_2:CO_2. TOS represents time-on-stream, R is the interatomic distance, CN is coordination number, and σ^2 is the mean square deviation in half-path-length. To reduce the contribution from noises and to compare spectra systematically, all spectra were fitted together sharing $\Delta E_0 = 5.95 \pm 0.34$ eV, reduced chi^2 = 9.84 and R factors = 2.20%. Additionally, same paths from different spectra share identical R and σ^2.

TOS (min)	Path	R (Å)	CN	σ^2(Å)
0	Ru-O	1.79 ± 0.01	0.14 ± 0.17	0.003 (set) for Ru-O 0.006 ± 0.000 for Ru-metal
	Ru-In	2.62 ± 0.01	0.61 ± 0.90	
	Ru-Ru	2.65 ± 0.00	6.25 ± 1.13	
0-20	Ru-O	1.79 ± 0.01	0.60 ± 0.36	
	Ru-In	2.62 ± 0.01	3.09 ± 1.87	
	Ru-Ru	2.65 ± 0.00	4.64 ± 2.26	
20-40	Ru-O	1.79 ± 0.01	0.60 ± 0.30	
	Ru-In	2.62 ± 0.01	2.52 ± 1.57	
	Ru-Ru	2.65 ± 0.00	6.26 ± 1.93	
40-60	Ru-O	1.79 ± 0.01	0.77 ± 0.37	
	Ru-In	2.62 ± 0.01	3.05 ± 1.90	
	Ru-Ru	2.65 ± 0.00	5.17 ± 2.31	
60-80	Ru-O	1.79 ± 0.01	0.76 ± 0.29	
	Ru-In	2.62 ± 0.01	4.47 ± 1.52	
	Ru-Ru	2.65 ± 0.00	3.56 ± 1.85	
80-100	Ru-O	1.79 ± 0.01	0.60 ± 0.33	
	Ru-In	2.62 ± 0.01	3.43 ± 1.70	
	Ru-Ru	2.65 ± 0.00	5.01 ± 2.08	
100-120	Ru-O	1.79 ± 0.01	0.63 ± 0.29	
	Ru-In	2.62 ± 0.01	3.68 ± 1.50	
	Ru-Ru	2.65 ± 0.00	3.69 ± 1.82	
120-140	Ru-O	1.79 ± 0.01	0.57 ± 0.31	
	Ru-In	2.62 ± 0.01	3.66 ± 1.59	
	Ru-Ru	2.65 ± 0.00	4.26 ± 1.92	
140-160	Ru-O	1.79 ± 0.01	0.48 ± 0.35	
	Ru-In	2.62 ± 0.01	1.94 ± 1.82	
	Ru-Ru	2.65 ± 0.00	6.41 ± 2.21	
160-180	Ru-O	1.79 ± 0.01	0.93 ± 0.38	
	Ru-In	2.62 ± 0.01	4.16 ± 1.98	
	Ru-Ru	2.65 ± 0.00	3.33 ± 2.39	

Table S2: Ru K-edge EXAFS fitting results of Ru/In_2O_3-ZrO_2 during CO_2 hydrogenation at 523 K, 6 bar, 20 ml·min^{-1} of 3:1 H_2:CO_2. TOS represents time-on-stream, R is the interatomic distance, CN is coordination number, and σ^2 is the mean square deviation in half-path-length. To reduce the contribution from noises and to compare spectra systematically, all spectra were fitted together sharing ΔE_0 = 1.79 ± 0.28 eV, reduced chi^2 = 11.46 and R factors = 3.21%. Additionally, same paths from different spectra share identical R and σ^2.

Edge	condition	Ru-In length (if included)	χ^2	reduced χ^2
Ru K	dry	2.62 +/- 0.01	880.78	11.46
		not included	1240.69	14.12
	wet	2.56 +/- 0.27	708.11	16.05
		not included	718.59	14.06
In K	dry	2.62 +/- 0.01	1058.18	15.24
		not included	1219.57	17.75
	wet	2.63 +/- 0.01	955.01	9.31
		not included	1182.18	10.41
Ru K (encapsulated)	wet	2.62 +/- 0.02	1022.91	23.52
		not included	1095.69	21.70
In K (encapsulated)	wet	2.66 +/- 0.06	1495.87	11.02
		not included	1780.43	11.89

Table S3: Ru and In K-edge EXAFS fitting results of Ru/In_2O_3-ZrO_2 during CO_2 hydrogenation at 523 K, 6 bar, 20 ml·min^{-1} of 3:1 H_2:CO_2 with or without the Ru-In scattering path. Fits that have the relatively smaller reduced χ^2 values were considered the optimal fit (highlighted in yellow in the table). It can be seen that including Ru-In paths were always statistically meaningful for XAS spectra collected under dry conditions for both Ru and In K edge, unambiguously confirming the presence of Ru-In alloy when catalyst deactivated under dry conditions. The reduced χ^2 values were however comparable if not smaller, when Ru-In paths were not included in the fit for spectra collected under 10% steam. This is strong evidence that the formation of Ru-In alloys was likely greatly, if not completely, suppressed when steam was used as a mild oxidant. However, for consistency and objectiveness, Ru-In paths were still included in the final fit which were reported in the manuscript.

TOS (min)	Path	R (Å)	σ^2(Å)	CN	
0	In-O	2.15 ± 0.00	0.010 ± 0.000	5.81 ± 0.17	
	In-In (1)	3.38 ± 0.00	0.008 ± 0.000	3.24± 0.36	4.00 ± 0.65
	In-In (2)	3.87 ± 0.00	0.005 ± 0.002	0.76 ± 0.29	
	In-Ru	2.63 ± 0.01	0.006 (set)	0.07 ± 0.13	
0-20	In-O	2.15 ± 0.00	0.010 ± 0.000	5.76 ± 0.12	
	In-In (1)	3.38 ± 0.00	0.008 ± 0.000	3.38 ± 0.24	3.92 ± 0.43
	In-In (2)	3.87 ± 0.00	0.005 ± 0.002	0.54 ± 0.19	
	In-Ru	2.63 ± 0.01	0.006 (set)	0.15 ± 0.08	
20-40	In-O	2.15 ± 0.00	0.010 ± 0.000	5.42 ± 0.12	
	In-In (1)	3.38 ± 0.00	0.008 ± 0.000	3.43 ± 0.25	3.94 ± 0.44
	In-In (2)	3.87 ± 0.00	0.005 ± 0.002	0.51 ± 0.19	
	In-Ru	2.63 ± 0.01	0.006 (set)	0.15 ± 0.08	
40-60	In-O	2.15 ± 0.00	0.010 ± 0.000	5.00 ± 0.11	
	In-In (1)	3.38 ± 0.00	0.008 ± 0.000	2.99 ± 0.22	3.23 ± 0.34
	In-In (2)	3.87 ± 0.00	0.005 ± 0.002	0.24 ± 0.12	
	In-Ru	2.63 ± 0.01	0.006 (set)	0.26 ± 0.07	
60-80	In-O	2.15 ± 0.00	0.010 ± 0.000	5.06 ± 0.13	
	In-In (1)	3.38 ± 0.00	0.008 ± 0.000	3.19 ± 0.28	3.63 ± 0.47
	In-In (2)	3.87 ± 0.00	0.005 ± 0.002	0.44 ± 0.19	
	In-Ru	2.63 ± 0.01	0.006 (set)	0.26 ± 0.10	
80-100	In-O	2.15 ± 0.00	0.010 ± 0.000	5.05 ± 0.11	
	In-In (1)	3.38 ± 0.00	0.008 ± 0.000	2.92 ± 0.23	3.42 ± 0.41
	In-In (2)	3.87 ± 0.00	0.005 ± 0.002	0.50 ± 0.18	
	In-Ru	2.63 ± 0.01	0.006 (set)	0.29 ± 0.08	
100-120	In-O	2.15 ± 0.00	0.010 ± 0.000	4.96 ± 0.11	
	In-In (1)	3.38 ± 0.00	0.008 ± 0.000	3.24 ± 0.23	3.81 ± 0.43
	In-In (2)	3.87 ± 0.00	0.005 ± 0.002	0.57 ± 0.20	
	In-Ru	2.63 ± 0.01	0.006 (set)	0.11 ± 0.08	
120-140	In-O	2.15 ± 0.00	0.010 ± 0.000	5.15 ± 0.13	
	In-In (1)	3.38 ± 0.00	0.008 ± 0.000	3.42 ± 0.28	4.03 ± 0.50
	In-In (2)	3.87 ± 0.00	0.005 ± 0.002	0.61 ± 0.22	
	In-Ru	2.63 ± 0.01	0.006 (set)	0.14 ± 0.10	
140-160	In-O	2.15 ± 0.00	0.010 ± 0.000	5.06 ± 0.11	
	In-In (1)	3.38 ± 0.00	0.008 ± 0.000	3.14 ± 0.24	3.59 ± 0.41
	In-In (2)	3.87 ± 0.00	0.005 ± 0.002	0.45 ± 0.17	
	In-Ru	2.63 ± 0.01	0.006 (set)	0.25 ± 0.08	
160-180	In-O	2.15 ± 0.00	0.010 ± 0.000	5.15 ± 0.12	
	In-In (1)	3.38 ± 0.00	0.008 ± 0.000	3.21 ± 0.25	3.93 ± 0.46
	In-In (2)	3.87 ± 0.00	0.005 ± 0.002	0.63 ± 0.21	
	In-Ru	2.63 ± 0.01	0.006 (set)	0.39 ± 0.08	

Table S4: In K-edge EXAFS fitting results of Ru/In_2O_3-ZrO_2 during CO_2 hydrogenation at 498 K, 6 bar, 20 ml·min^{-1} of 3:1 H_2:CO_2 and 10% added steam. TOS represents time-on-stream, R is the

interatomic distance, CN is coordination number, and σ^2 is the mean square deviation in half-path-length. To reduce the contribution from noises and to compare spectra systematically, all spectra were fitted together sharing $\Delta E_0 = 7.07 \pm 0.16$ eV, reduced $chi^2 = 7.71$ and R factors = 0.69%. Additionally, same paths from different spectra share identical R and σ^2.

TOS (min)	Path	R (Å)	CN	σ^2(Å)
0	Ru-O	1.78 ± 0.05	0.19 ± 0.28	0.003 (set) for Ru-O 0.006 ± 0.000 for Ru-metal
	Ru-In	2.56 ± 0.27	0.02 ± 0.77	
	Ru-Ru	2.65 ± 0.00	8.18 ± 1.07	
0-36	Ru-O	1.78 ± 0.05	0.11 ± 0.26	
	Ru-In	2.56 ± 0.27	0.00 ± 0.76	
	Ru-Ru	2.65 ± 0.00	8.09 ± 1.07	
36-72	Ru-O	1.78 ± 0.05	0.10 ± 0.31	
	Ru-In	2.56 ± 0.27	0.30 ± 1.17	
	Ru-Ru	2.65 ± 0.00	8,12 ± 1.84	
72-108	Ru-O	1.78 ± 0.05	0.27 ± 0.22	
	Ru-In	2.56 ± 0.27	0.00 ± 0.72	
	Ru-Ru	2.65 ± 0.00	8.24 ± 1.03	
108-144	Ru-O	1.78 ± 0.05	0.12 ± 0.28	
	Ru-In	2.56 ± 0.27	0.00 ± 0.78	
	Ru-Ru	2.65 ± 0.00	8.19 ± 1.10	
144-180	Ru-O	1.78 ± 0.05	0.21 ± 0.25	
	Ru-In	2.56 ± 0.27	0.14 ± 0.76	
	Ru-Ru	2.65 ± 0.00	7.95 ± 1.11	

Table S5: Ru K-edge EXAFS fitting results of Ru/In_2O_3-ZrO_2 during CO_2 hydrogenation at 498 K, 6 bar, 20 ml·min^{-1} of 3:1 H_2:CO_2 and 10% added steam. TOS represents time-on-stream, R is the interatomic distance, CN is coordination number, and σ^2 is the mean square deviation in half-path-length. To reduce the contribution from noises and to compare spectra systematically, all spectra were fitted together sharing ΔE_0 = 1.00 ± 0.36 eV, reduced chi^2 = 16.40 and R factors = 2.05%. Additionally, same paths from different spectra share identical R.

TOS (min)	Path	R (Å)	σ^2(Å)	CN	
0	In-O	2.14 ± 0.00	0.010 ± 0.000	6.20 ± 0.23	
	In-In (1)	3.37 ± 0.00	0.008 ± 0.000	3.77± 0.50	4.59 ± 1.00
	In-In (2)	3.85 ± 0.01	0.005 ± 0.002	0.82 ± 0.50	
	In-Ru	2.62 ± 0.02	0.006 (set)	0.04 ± 0.17	
0-20	In-O	2.14 ± 0.00	0.010 ± 0.000	5.87 ± 0.16	
	In-In (1)	3.37 ± 0.00	0.008 ± 0.000	3.43 ± 0.33	4.48 ± 0.71
	In-In (2)	3.85 ± 0.01	0.005 ± 0.002	1.05 ± 0.38	
	In-Ru	2.62 ± 0.02	0.006 (set)	0.00 ± 0.10	
20-40	In-O	2.14 ± 0.00	0.010 ± 0.000	5.82 ± 0.14	
	In-In (1)	3.37 ± 0.00	0.008 ± 0.000	3.31 ± 0.28	3.94 ± 0.44
	In-In (2)	3.85 ± 0.01	0.005 ± 0.002	0.83 ± 0.30	
	In-Ru	2.62 ± 0.02	0.006 (set)	0.03 ± 0.08	
40-60	In-O	2.14 ± 0.00	0.010 ± 0.000	5.83 ± 0.14	
	In-In (1)	3.37 ± 0.00	0.008 ± 0.000	3.56 ± 0.30	3.23 ± 0.34
	In-In (2)	3.85 ± 0.01	0.005 ± 0.002	1.34 ± 0.41	
	In-Ru	2.62 ± 0.02	0.006 (set)	0.10 ± 0.09	
60-80	In-O	2.14 ± 0.00	0.010 ± 0.000	5.73 ± 0.14	
	In-In (1)	3.37 ± 0.00	0.008 ± 0.000	3.35 ± 0.30	3.63 ± 0.47
	In-In (2)	3.85 ± 0.01	0.005 ± 0.002	0.84 ± 0.32	
	In-Ru	2.62 ± 0.02	0.006 (set)	0.12 ± 0.09	
80-100	In-O	2.14 ± 0.00	0.010 ± 0.000	5.73 ± 0.18	
	In-In (1)	3.37 ± 0.00	0.008 ± 0.000	3.30 ± 0.37	3.42 ± 0.41
	In-In (2)	3.85 ± 0.01	0.005 ± 0.002	1.14 ± 0.44	
	In-Ru	2.62 ± 0.02	0.006 (set)	0.14 ± 0.13	
100-120	In-O	2.14 ± 0.00	0.010 ± 0.000	5.69 ± 0.15	
	In-In (1)	3.37 ± 0.00	0.008 ± 0.000	3.30 ± 0.20	3.81 ± 0.43
	In-In (2)	3.85 ± 0.01	0.005 ± 0.002	1.14 ± 0.37	
	In-Ru	2.62 ± 0.02	0.006 (set)	0.23 ± 0.09	
120-140	In-O	2.14 ± 0.00	0.010 ± 0.000	5.82 ± 0.17	
	In-In (1)	3.37 ± 0.00	0.008 ± 0.000	3.06 ± 0.34	4.03 ± 0.50
	In-In (2)	3.85 ± 0.01	0.005 ± 0.002	1.00 ± 0.39	
	In-Ru	2.62 ± 0.02	0.006 (set)	0.23 ± 0.11	
140-160	In-O	2.14 ± 0.00	0.010 ± 0.000	5.73 ± 0.18	
	In-In (1)	3.37 ± 0.00	0.008 ± 0.000	3.46 ± 0.38	3.59 ± 0.41
	In-In (2)	3.85 ± 0.01	0.005 ± 0.002	1.18 ± 0.45	
	In-Ru	2.62 ± 0.02	0.006 (set)	0.13 ± 0.13	
160-180	In-O	2.14 ± 0.00	0.010 ± 0.000	5.79 ± 0.16	
	In-In (1)	3.37 ± 0.00	0.008 ± 0.000	3.49 ± 0.34	3.93 ± 0.46
	In-In (2)	3.85 ± 0.01	0.005 ± 0.002	1.08 ± 0.39	
	In-Ru	2.62 ± 0.02	0.006 (set)	0.15 ± 0.10	

Table S6: In K-edge EXAFS fitting results of IPOP/Ru/In_2O_3-ZrO_2 during CO_2 hydrogenation at 498 K, 6 bar, 20 ml·min^{-1} of 3:1 H_2:CO_2 and 10% added steam. TOS represents time-on-stream,

R is the interatomic distance, CN is coordination number, and σ^2 is the mean square deviation in half-path-length. To reduce the contribution from noises and to compare spectra systematically, all spectra were fitted together sharing $\Delta E_0 = 5.65 \pm 0.20$ eV, reduced $chi^2 = 12.16$ and R factors = 0.81%. Additionally, same paths from different spectra share identical R and σ^2.

TOS (min)	Path	R (Å)	CN	σ^2(Å)
0	Ru-O	1.83 ± 0.03	0.38 ± 0.31	0.003 (set) for Ru-O 0.005 ± 0.001 for Ru-metal
	Ru-In	2.66 ± 0.06	0.88 ± 1.06	
	Ru-Ru	2.66 ± 0.01	6.93 ± 1.35	
0-36	Ru-O	1.83 ± 0.03	0.36 ± 0.37	
	Ru-In	2.66 ± 0.06	1.17 ± 1.09	
	Ru-Ru	2.66 ± 0.01	6.71 ± 1.34	
36-72	Ru-O	1.83 ± 0.03	0.50 ± 0.28	
	Ru-In	2.66 ± 0.06	0.95 ± 0.96	
	Ru-Ru	2.66 ± 0.01	6.75 ± 1.23	
72-108	Ru-O	1.83 ± 0.03	0.20 ± 0.31	
	Ru-In	2.66 ± 0.06	1.54 ± 0.97	
	Ru-Ru	2.66 ± 0.01	6.94 ± 1.26	
108-144	Ru-O	1.83 ± 0.03	0.17 ± 0.37	
	Ru-In	2.66 ± 0.06	0.82 ± 1.12	
	Ru-Ru	2.66 ± 0.01	6.70 ± 1.41	
144-180	Ru-O	1.83 ± 0.03	0.38 ± 0.25	
	Ru-In	2.66 ± 0.06	1.25 ± 0.82	
	Ru-Ru	2.66 ± 0.01	6.41 ± 1.07	

Table S7: Ru K-edge EXAFS fitting results of IPOP/Ru/In_2O_3-ZrO_2 during CO_2 hydrogenation at 498 K, 6 bar, 20 ml·min^{-1} of 3:1 H_2:CO_2 and 10% added steam. TOS represents time-on-stream, R is the interatomic distance, CN is coordination number, and σ^2 is the mean square deviation in half-path-length. To reduce the contribution from noises and to compare spectra systematically, all spectra were fitted together sharing $\Delta E_0 = 2.35 \pm 0.48$ eV, reduced $chi^2 = 23.52$ and R factors = 2.43%. Additionally, same paths from different spectra share identical R.

ref.	year	phase	catalyst	P (Mpa)	T (K)	Conv. (%)	Selectivity (%)				Ethanol Yield (%)	Space-Time Yield (mg/g/h)	H_{eff} (%)
							hydrocarbons	oxygenates					
								CO	CH_3OH	$C_{2+}OH$			
1	2018	L	Co/AlO_x-600	4	413	N/A	0	0	8	92	N/A	20	92
2	2017	L	Pd_2Cu/P25	3.2	473	N/A	0	0	8	92	N/A	1912	92
this work	2023	G	Ru/In_2O_3-ZrO_2	0.6	498	8	0	30	0	70	6	26	88
3	2020	G	Cu@Na-Beta	1.3	573	8	0	31	0	70	6	156	87
4	2022	G	$In_xFe_{2-x}O_3$/K	2	573	37	48	7	3	42	15	N/A	41
5	2013	G	$CuZnFe_{0.5}K_{0.15}$	6	573	42	56	7	5	32	14	148	28
6	2016	L	Co/Mo_2C	4	473	N/A	17	10	46	25	N/A	N/A	26
7	2016	L	Pt/Co_3O_4	8	493	N/A	67	0	4	29	N/A	0.3	24
8	2022	G	K-CuFeZn	5	593	34	68	12	0	20	7	51	21
9	2022	G	$Cu\text{-}CoGaO_{0.4}$	3	493	18	48	0	29	24	4	62	21
10	2021	G	CuZnAl + K-CuMgZnFe	5	593	42	68	14	1	17	7	107	19
11	2011	G	CoMoS	10.3	583	17	5	69	22	4	1	N/A	8

Table S8: Catalyst performances from relevant studies. Catalysis performed in liquid under discontinuous batch conditions were labeled in blue. Hydrogen efficiency (H_{eff}) is defined as

$$Hydrogen\ efficiency\ (\%) = \frac{amount\ of\ hydrogen\ consumed\ to\ produce\ C_2H_5OH}{amount\ moles\ of\ hydrogen\ consumed\ by\ CO_2} \times 100\%$$

For example, for our catalyst that produced 30% CO and 70% ethanol, the hydrogen efficiency (H_{eff}) is:

$$CO_2 + 3H_2 \rightarrow \frac{1}{2}C_2H_5OH + \frac{3}{2}H_2O$$

$$CO_2 + H_2 \rightarrow CO + H_2O$$

$$H_{eff}\ (\%) = \frac{70\% \times 3}{30\% \times 1 + 70\% \times 3} \times 100\% = 87.5\%$$

For a catalyst producing 50% ethanol and 50% methane (similar to ref 4), the hydrogen efficiency becomes:

$$CO_2 + 3H_2 \rightarrow \frac{1}{2}C_2H_5OH + \frac{3}{2}H_2O$$

$$CO_2 + 4H_2 \rightarrow CH_4 + 2H_2O$$

$$H_{eff}\ (\%) = \frac{50\% \times 3}{50\% \times 4 + 50\% \times 3} \times 100\% = 42.9\%$$

Basically, the hydrogen atomic efficiency informs us about the overall selectivity of the reaction as normalized by conversion. Our work indeed represents the highest hydrogen efficiency for continuous gas-phase production of ethanol from CO_2 hydrogenation owing to the high selectivity towards ethanol and the absence of hydrocarbon side-products.

References

1. Wang, *et al*. Selective hydrogenation of CO_2 to ethanol over cobalt catalysts. *Angew Chem Int Ed* **57**, 6104-6108 (2018).
2. Bai, *et al*. Highly active and selective hydrogenation of CO_2 to ethanol by ordered Pd–Cu nanoparticles. *JACS* **139**, 6827-6830 (2017).
3. Ding, *et al*. CO_2 hydrogenation to ethanol over Cu@ Na-Beta. *Chem* **6**, 2673-2689 (2020).
4. Goud, *et al*. Strain-Enhanced Phase Transformation of Iron Oxide for Higher Alcohol Production from CO_2. *ACS Catalysis* **12**, 11118-11128 (2022).
5. Li, *et al*. Effect of iron promoter on structure and performance of K/Cu–Zn catalyst for higher alcohols synthesis from CO_2 hydrogenation. *Catalysis letters* **143**, 345-355 (2013).
6. Chen, *et al*. Low temperature CO_2 hydrogenation to alcohols and hydrocarbons over Mo_2C supported metal catalysts. *Journal of catalysis* **343**, 147-156 (2016).
7. He, *et al*. Water-enhanced synthesis of higher alcohols from CO_2 hydrogenation over a Pt/Co_3O_4 catalyst under Milder conditions. *Angew Chem Int Ed* **55**, 737-741 (2016).
8. Wang, *et al*. Sulfate-Promoted Higher Alcohol Synthesis from CO_2 Hydrogenation. *ACS Sustainable Chem Eng* **10**, 8980-8987 (2022).
9. Zhang, *et al*. Ga-Promoted CuCo-Based Catalysts for Efficient CO_2 Hydrogenation to Ethanol: The Key Synergistic Role of Cu-$CoGaO_x$ Interfacial Sites. *ACS Appl Mat & Interfaces* **14**, 35569-35580 (2022).
10. Xu, *et al*. Tandem catalysis of direct CO_2 hydrogenation to higher alcohols. *ACS Catalysis* **11**, 8978-8984 (2021).
11. Nieskens, *et al*. The conversion of carbon dioxide and hydrogen into methanol and higher alcohols. *Catalysis Communications* **14**, 111-113 (2011).